

EXPLORING THE NUCLEAR STRUCTURE
OF ^{77}Se VIA INELASTIC DEUTERON
SCATTERING

by

J. Alex Harget

© Copyright by J. Alex Harget, 2017

All Rights Reserved

A thesis submitted to the Faculty and the Board of Trustees of the Colorado School of Mines in partial fulfillment of the requirements for the degree of Master of Science (Applied Physics).

Golden, Colorado

Date _____

Signed: _____
J. Alex Harget

Signed: _____
Dr. Kyle Leach
Thesis Advisor

Golden, Colorado

Date _____

Signed: _____
Dr. Jeff Squier
Professor and Head
Department of Physics

ABSTRACT

The weak process of nuclear double beta decay presents an opportunity to explore the nature of the neutrino as well as the conservation of lepton number. These studies perhaps provide one of the best avenues for investigating physical concepts beyond the Standard Model (BSM) of particle physics. One such study is the proposed neutrinoless double beta decay of $^{76}\text{Ge} \rightarrow ^{76}\text{Se}$. Studies into nearby systems can offer insight into the nature of this process. In particular, computation of the nuclear matrix elements (NMEs) is necessary to predict the half-life of this decay, which subsequently reveals the mass characteristics of the neutrino. The NME calculation methods for the $A = 76$ transition can be benchmarked to the 1-neutron removed ^{77}Se nucleus by characterizing the nuclear properties of the latter and using this to assess and refine the model used in the analysis of the former.

To this end, an inelastic scattering experiment of deuterons on ^{77}Se was performed at the Maier-Leibnitz Laboratory in Garching, Germany at angles ranging from 5° to 115° in increments of 5° . A total of nine nuclear states were populated and the corresponding angular cross section distributions were obtained. These angular distributions were then compared to coupled-channel calculations and 14 nuclear β deformation parameters were extracted for ^{77}Se . These parameters reveal information about the deformation of the nucleus for each state, which motivates future work in the study of the $0\nu\beta\beta$ decay mode and ultimately of the Standard Model.

TABLE OF CONTENTS

ABSTRACT	iii
LIST OF FIGURES	vi
LIST OF TABLES	viii
LIST OF ABBREVIATIONS	ix
ACKNOWLEDGMENTS	x
DEDICATION	xi
CHAPTER 1 INTRODUCTION TO β DECAY AND NUCLEAR STRUCTURE	1
1.1 β Decay	1
1.2 $\beta\beta$ Decay	2
1.3 Neutrinoless $\beta\beta$ Decay	3
1.3.1 The Majorana Mass of the Neutrino	4
1.4 Experimental Tests of Nuclear Structure Theory	5
1.5 The $\beta\beta$ Decay of ${}^{76}\text{Ge} \rightarrow {}^{76}\text{Se}$	6
CHAPTER 2 EXPERIMENT	7
2.1 ${}^{77}\text{Se}(\text{d},\text{d}'){}^{77}\text{Se}$ Scattering Experiment	7
2.1.1 Elastic Scattering	7
2.1.2 Inelastic Scattering	9
2.2 Experimental Facility	9
2.3 Experimental Energy Spectra	13
2.4 Cross Section Extraction	16

2.5	Cross Section Normalization	19
2.6	Energy Calibration	22
CHAPTER 3 COUPLED-CHANNEL CALCULATIONS WITH FRESCO		24
3.1	Scattering Theory	24
3.1.1	The Distorted-Wave Born Approximation	25
3.1.2	The Optical Model	26
3.2	FRESCO	29
3.3	SFRESCO	32
3.4	Extraction of β Deformation Parameters	33
CHAPTER 4 DISCUSSION AND CONCLUSIONS		35
4.1	Extracted β Deformation Parameters	35
4.2	State-by-State Discussion	36
4.3	Conclusions	42
REFERENCES CITED		45
APPENDIX EXPERIMENTAL ENERGY SPECTRA		47

LIST OF FIGURES

Figure 1.1	Mass Parabolas for Odd- and Even- A Nuclei	2
Figure 1.2	Feynman Diagram for Proposed Neutrinoless Double Beta Decay	5
Figure 2.1	Schematic of Inelastic Deuteron Scattering from ^{77}Se	7
Figure 2.2	Kinematic Elastic Scattering Curves	8
Figure 2.3	Kinematic Inelastic Scattering Curves	10
Figure 2.4	Tandem Hall at the MLL	10
Figure 2.5	Schematic of Van de Graaff Generator	11
Figure 2.6	Experimental Target Ladder	12
Figure 2.7	Q3D Magnetic Spectrograph	13
Figure 2.8	Complete Experimental Beam Path	14
Figure 2.9	Impurity Scattering on the Focal Plane	16
Figure 2.10	Normalization Procedure Applied	20
Figure 2.11	85° Run Cross Section Behavior	20
Figure 2.12	Experimental Angular Distributions	21
Figure 2.13	Linear Focal Plane Calibration Scheme	22
Figure 3.1	The Woods-Saxon Potential and Derivative	27
Figure 3.2	Cross Section Comparison of Four Global OMP Sets	30
Figure 3.3	FRESCO Input File	31
Figure 3.4	FRESCO Ground State <i>fort.201</i> File	32
Figure 3.5	SFRESCO <i>.search</i> File	33

Figure 3.6	SFRESCO <i>search.plot</i> File	34
Figure 4.1	β Parameter Coupling Scheme	35
Figure 4.2	Removal of 5° Data Point	37
Figure 4.3	Unresolved 239, 250 keV Doublet	39
Figure 4.4	Experimental Distributions and Calculations	43

LIST OF TABLES

Table 1.1	Observed $2\nu\beta\beta$ Decay Half-lives	3
Table 2.1	Integrated Sums of Nine Peaks	15
Table 2.2	Experimental Parameters for Cross Section Extraction	18
Table 2.3	Experimentally-Populated State Assignment	23
Table 3.1	Four Global OMP Sets Considered for Use in SFRESCO	29
Table 4.1	Extracted β Values Compared to Literature	36

LIST OF ABBREVIATIONS

Distorted-wave Born approximation	DWBA
Neutrinoless double beta decay	$0\nu\beta\beta$
Nuclear matrix element	NME
Beyond the standard model	BSM
Maier-Leibnitz laboratory	MLL
Quadrupole-3-dipole	Q3D
Application-specific integrated circuits	ASICs
Data acquisition	DAQ
Center of mass	CM

ACKNOWLEDGMENTS

I extend my full gratitude to my advisor Kyle Leach, and colleagues, Connor Natzke and Hannah Grover, for traveling to Germany and completing the experiment. It's been great working together in our EI group. Dr. Leach, it's been a pleasure working on this project with you (as well as in taking and TAing your class) and I fully appreciate your perfect blend of practicality, kindness and competence, qualities that make any project that much more enjoyable to complete. I also appreciate the encouragement and provision from my parents, Jim and Dara, who have been excellent supporters from day one, as well as the enjoyment from friends new and old. I wouldn't be here otherwise and it's my pleasure to share the culmination of these contributions through this work.

I can do all things through Christ which strengtheneth me.

~Philippians 4:13

CHAPTER 1
INTRODUCTION TO β DECAY AND NUCLEAR STRUCTURE

1.1 β Decay

Nuclear β decay is a weak process in which a bound neutron is converted into a proton (called β^- decay),

$$n \rightarrow p + e^- + \bar{\nu}_e \quad (1.1)$$

or a bound proton into a neutron (β^+ decay),¹

$$p \rightarrow n + e^+ + \nu_e. \quad (1.2)$$

An electron and electron antineutrino ($\bar{\nu}_e$) are emitted in β^- decay and a positron and electron neutrino (ν_e) in β^+ decay. The neutrino and antineutrino balance lepton number across the decay and carry away some of the energy of the process.

To first order, this process is allowed only so long as it decreases the mass of the system. The masses of the nuclei are modeled with the *semiempirical mass formula*:

$$M(Z, A) = Zm_p + Nm_n - E_B/c^2 \quad (1.3)$$

$$E_B = a_v A - a_s A^{2/3} - a_c Z(Z-1)A^{-1/3} - a_A \frac{(A-2Z)^2}{A} + \delta(A, Z),$$

where m_p and m_n are the masses of the proton and neutron, respectively, E_B is the binding energy of the system, and a_v , a_s , a_c , a_A , and $\delta(A, Z)$ are determined experimentally [1]. By holding A constant and plotting the nuclear masses as a function of Z , we obtain a parabola centered around the minimum mass for a given A value. β decay moves the nucleus down this parabola, one step at a time, closer to stability. The nucleus at the bottom of the parabola is said to be *β decay-stable* because there is no location below it to which it can decay. For even- A nuclei, there are two parabolas that result: one for odd-odd nuclei and

¹Only bound protons, and not free protons, exhibit this decay behavior because of interactions with other particles in the nucleus.

one for even-even nuclei. This leads to some unique features. For example, a single β decay process requires a jump from one parabola to the other (because the net change in nucleons is singular), but this can only happen if the overall movement in the direction of the mass axis is downward. If such a movement increases the mass, this process is not allowed to first order in the β -decay process.

1.2 $\beta\beta$ Decay

In a few nuclear systems, single beta decay does not result in an increase in the system's binding energy, however, a second-order weak process can be considered. In certain systems, it is possible to undergo *double beta decay* ($\beta\beta$) and simultaneously convert two neutrons to two protons or vice versa. Being second-order in the weak interaction, however, this process is suppressed by many orders of magnitude. An example of the energetics of this process as it compares to single β decay is shown in Figure 1.1.

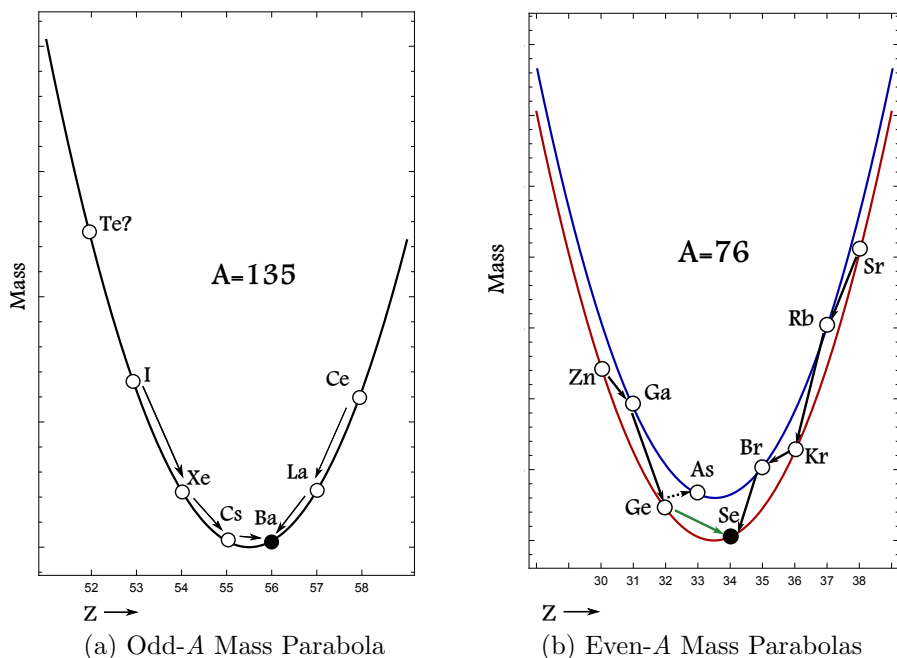


Figure 1.1: Mass parabolas for (a) odd- A and (b) even- A nuclei. Two parabolas result for the even- A case due to the pairing term in the semiempirical mass formula, $\delta(A,Z)$. The odd- A case does not allow for $\beta\beta$ decay. The even- A case, however, requires ^{76}Ge to double beta decay to ^{76}Se , for example, by skipping the otherwise inaccessible state in ^{76}As .

12 nuclei have been experimentally observed to undergo $\beta^-\beta^-$ decay [2], for which there are two modes: two-neutrino (2ν) and neutrinoless (0ν). $2\nu\beta\beta$ decay is an allowed process in the Standard Model and facilitates the conversion of two neutrons into protons with the emission of a pair of beta particles (electrons for β^- decay) and a pair of electron antineutrinos:

$${}^A_Z W_N \rightarrow {}^A_{Z+2} Y_{N-2} + 2e^- + 2\bar{\nu}_e. \quad (1.4)$$

The typical half-lives of this process fall between 10^{19} and 10^{25} years, as shown in Table 1.1.

Table 1.1: Half-lives for the 12 observed nuclides to undergo $2\nu\beta\beta$ decay according to [2]. When two errors are listed, the first is the statistical uncertainty and the second is systematic. Two geochemical measurements are given for ${}^{128}\text{Te}$.

Nuclide	$t_{1/2}$ (10^{19} yr)
${}^{48}\text{Ca}$	$4.4^{+0.5}_{-0.4} \pm 0.4$
${}^{76}\text{Ge}$	192.6 ± 9.4
${}^{78}\text{Kr}$	$920^{+550}_{-260} \pm 130$
${}^{82}\text{Se}$	$9.6 \pm 0.3 \pm 1.0$
${}^{96}\text{Zr}$	$2.35 \pm 0.14 \pm 0.16$
${}^{100}\text{Mo}$	0.693 ± 0.04
${}^{116}\text{Cd}$	$2.8 \pm 0.1 \pm 0.3$
${}^{128}\text{Te}$	$720,000 \pm 40,000$ $180,000 \pm 70,000$
${}^{130}\text{Te}$	$69 \pm 9 \pm 10$
${}^{136}\text{Xe}$	$216.5 \pm 1.6 \pm 5.9$
${}^{150}\text{Nd}$	$0.911^{+0.025}_{-0.022} \pm 0.063$
${}^{238}\text{U}$	200 ± 60

1.3 Neutrinoless $\beta\beta$ Decay

Unlike $2\nu\beta\beta$ decay, the 0ν mode of this decay process is not allowed by the Standard Model, and in fact requires two extensions in order to be modeled if it were found. Firstly, without the emission of neutrinos, this process causes a change in lepton number (+2). Therefore, if the $0\nu\beta\beta$ mode were ever observed, any new extension to the Standard Model

would have to allow processes that violate lepton conservation, thereby showing that lepton “charge” is not a conserved quantum number. Secondly, the neutrino could not be a Dirac fermion, as is the case for all other fundamental fermions in the standard model, but rather it would have to be its own antiparticle: a *Majorana fermion*. The $0\nu\beta\beta$ process can be thought of as a pair of beta decay processes across the intermediate state wherein the neutrino is virtually annihilated [1]. This intermediate state is energetically inaccessible to single β decay and thus this intermediate process occurs virtually. In order for the neutrino leaving the first decay to be absorbed by the second, it must be its own antiparticle in the following process:

$${}^A_Z W_N \rightarrow {}^A_{Z+1} X_{N-1} + e^- + \bar{\nu}_e \quad (1.5)$$

$$\nu_e + {}^A_{Z+1} X_{N-1} \rightarrow {}^A_{Z+2} Y_{N-2} + e^-, \quad (1.6)$$

where the antineutrino in the first phase is the same as the neutrino absorbed (virtually) in the second. This proposed process is illustrated in the Feynman diagram of Figure 1.2. The equivalence of the neutrino with the antineutrino is not permissible with a massless neutrino¹ and therefore it must have a “Majorana mass” component for this equivalence to hold. It has been found, via neutrino oscillations, that the neutrino does in fact have a mass [3, 4]. Therefore, this process has become an area of active study.

1.3.1 The Majorana Mass of the Neutrino

If the $0\nu\beta\beta$ decay mode were to be observed, the effective Majorana mass of the neutrino, $\langle m_{\beta\beta} \rangle$, can be deduced from the measured half-life of the reaction according to

$$(T_{1/2}^{0\nu})^{-1} = G^{0\nu}(Q, Z) |M^{0\nu}|^2 \langle m_{\beta\beta} \rangle^2, \quad (1.7)$$

where $T_{1/2}^{0\nu}$ is the observed half-life of the $0\nu\beta\beta$ decay and $G^{0\nu}$ is a phase-space factor [5]. $M^{0\nu}$ is the nuclear matrix element that connects the initial and final 0^+ states, a product solely of theoretical calculations. If a half-life were to be experimentally measured, reliable

¹Nor can the helicity of the neutrino be definite [1].

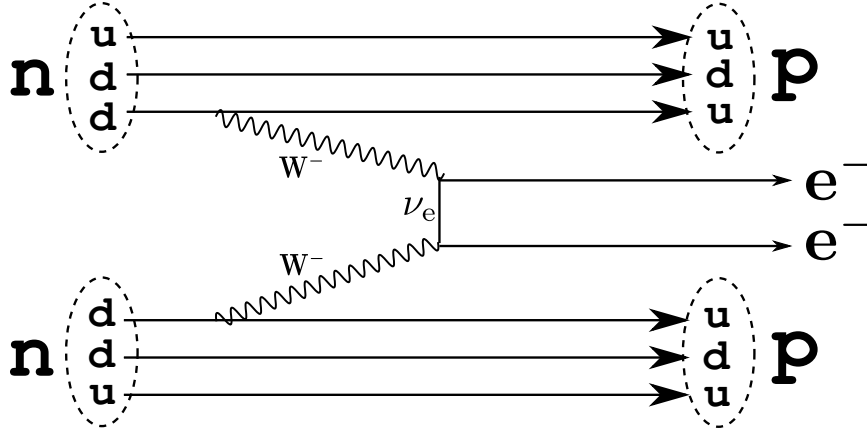


Figure 1.2: Feynman diagram of the proposed $0\nu\beta\beta$ decay process, which converts two neutrons into two protons and emits two electrons. Instead of emitting two neutrinos (as in $2\nu\beta\beta$ decay), a single virtual neutrino is emitted by the first half of the process and absorbed by the second half. This can only happen if the electron neutrino is its own antiparticle.

NMEs must be entered into Equation 1.7 to compute the Majorana mass of the neutrino. The computation of $\beta\beta$ decay NMEs is the source of many current theoretical efforts and has led to multiple different model descriptions.

One approach utilizes the nuclear shell model, which does a good job of accurately describing nuclear masses and lower excited states. However, using the shell model to determine NMEs only treats higher-energy orbitals as perturbations to the lower-lying ones because most efforts have only used a single harmonic-oscillator shell as the configuration space [5]. This yields lower values for the NMEs than some of the other current models, although other causes for discrepancies are still being investigated. The inclusion of nuclear structure interactions (such as those of nucleon pairing), however, increases the magnitude of the resultant NMEs because such scenarios tend to favor the 0ν mode. In order to reliably calculate the NMEs, experimental nuclear structure guidance in these systems is critical.

1.4 Experimental Tests of Nuclear Structure Theory

The theoretical models that are employed in calculating double beta decay NMEs yield dramatically different results. In fact, the differences are so large that the extracted Majorana mass, $\langle m_{\beta\beta} \rangle$, for a given half-life can vary by nearly an order of magnitude [5]. As a result,

experimental data in the region of the nuclear chart close to the $\beta\beta$ decaying nuclei are required to provide rigorous tests of each model.

Nuclear scattering experiments serve as an excellent probe of the nuclear shape, as they are sensitive to small deviations of the ground state wave function present in the excited states. These shapes are quantified by nuclear β deformation parameters which are intimately tied to the transition probabilities between initial and final states, $B(E\lambda; i \rightarrow f)$, where $E\lambda$ is an electric transition of multipolarity λ (see section 4.1). These quantities give explicit information about the form of the wave function for each state and therefore are used to classify each state's nuclear shape.

1.5 The $\beta\beta$ Decay of $^{76}\text{Ge} \rightarrow ^{76}\text{Se}$

One of the most promising candidates for a direct observation of the $0\nu\beta\beta$ mode is ^{76}Ge , whose daughter nucleus is ^{76}Se . Tests are already underway to find the neutrinoless mode in this isotope, however, no peak has been found thus far [6]. Lower limits on the half-life of this mode have been reported, however, with Ref. [6] yielding, in combination with other experiments, $T_{1/2}^{0\nu} > 3.0 \times 10^{25}$ yr (90% C.L.). This long half-life means that large samples of enriched germanium must be analyzed over a long period of time to observe an appreciable amount of events at the detector. Since ^{77}Se is only one neutron away from the daughter nucleus of the decay above, ^{76}Se , classifying the structure of the former can help refine theoretical models for the above germanium $\beta\beta$ decay. This Thesis reports the determination of the low-lying nuclear shapes in ^{77}Se via inelastic deuteron scattering.

CHAPTER 2
EXPERIMENT

2.1 $^{77}\text{Se}(d,d')^{77}\text{Se}$ Scattering Experiment

The reaction studied in this Thesis is inelastic deuteron scattering on ^{77}Se , notated $^{77}\text{Se}(d,d')^{77}\text{Se}$. The incoming deuterons are referred to as the *projectiles*, and the outgoing deuterons as the *ejectiles*. Note that in scattering experiments, these are the same particle, and only the energy of the projectile changes. The stationary ^{77}Se is the *target* and following the reaction, it is called the *recoil* nucleus. This reaction is shown in Figure 2.1 with the masses, energies, and angles notated.

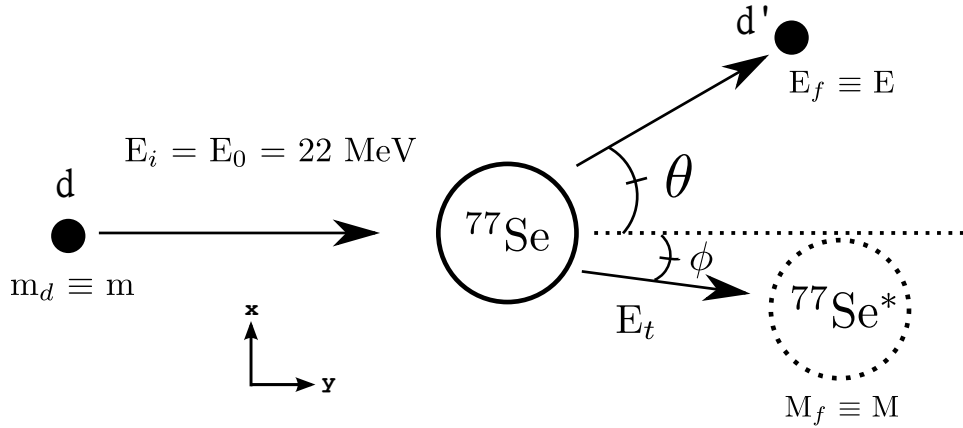


Figure 2.1: A schematic of inelastic deuteron scattering from ^{77}Se . The deuterons leave with a different energy as a result of kinematic losses and the excitation of the nucleus.

2.1.1 Elastic Scattering

Treating the reaction purely classically is an exercise in conservation of four-momentum: $\vec{P}_0 = \vec{P}_f$. This equation becomes (the notation of which is presented in Figure 2.1):

$$\begin{pmatrix} E_0/c \\ \sqrt{2mE_0} \\ 0 \end{pmatrix} = \begin{pmatrix} (E + E_t)/c \\ \sqrt{2mE} \cos \theta + \sqrt{2ME_t} \cos \phi \\ \sqrt{2mE} \sin \theta + \sqrt{2ME_t} \sin \phi \end{pmatrix}, \quad (2.1)$$

where the x-axis is aligned with the direction of projectile motion and there are no contributions in the z-direction. The classical substitution $p = \sqrt{2mE}$ was also made. The solution to these coupled equations for the ejectile energy, E , as a function of the angle of scattering, θ , is

$$E(\theta) = \frac{2m^2 E_0 \cos^2(\theta) - E_0(m^2 - M^2) \pm 2mE_0 \cos(\theta) \sqrt{m^2 \cos^2(\theta) - m^2 + M^2}}{(M + m)^2} \quad (2.2)$$

This classical formulation only depends on the projectile mass, projectile energy and target mass. Figure 2.2 shows Equation 2.2 plotted for various values of target mass, namely select oxygen, nitrogen and selenium isotopes. The latter element is present in the target in the form of impurities and the former two molecules are common impurities from the ambient air that accumulate on the targets before they are placed into the experimental chamber.

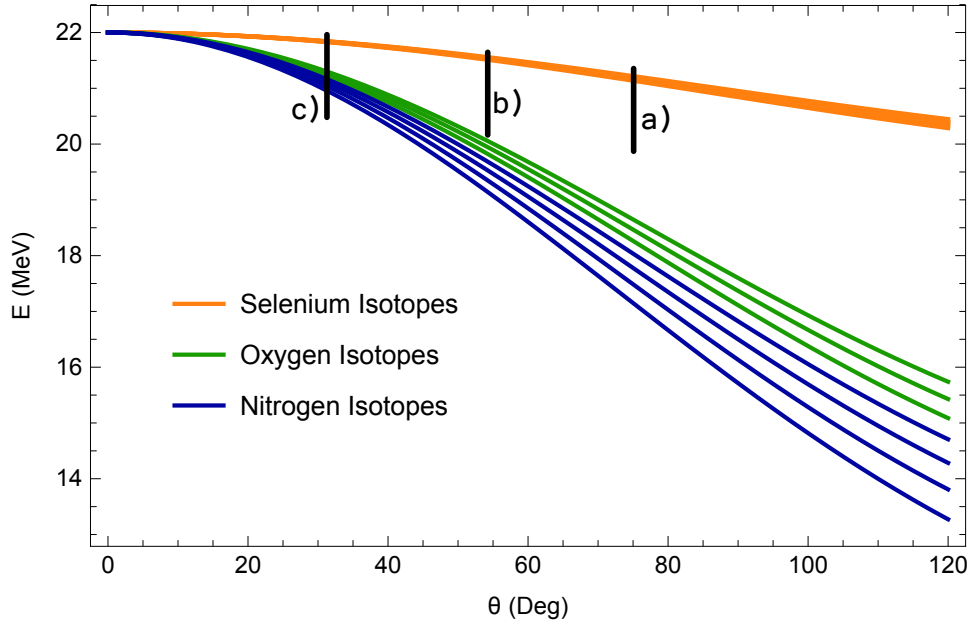


Figure 2.2: Equation 2.2 plotted for various target masses that correspond to selenium, oxygen and nitrogen isotopes. The black bars represent the approximate energy range coverage of the focal plane detector in this experiment (~ 1.5 MeV). In a), only the desired events are seen because scattering on the impurities is at an energy level that is not detected at the focal plane. Unwanted events begin to appear at approximately 55 degrees at b), and at c), they have fully entered the focal plane, enveloping certain peaks of interest and also demanding an adjusted beam current.

2.1.2 Inelastic Scattering

To address the population of excited states via inelastic scattering, a change in the ejectile energy is required. The energy absorbed by the nucleus leads to an increased target mass. As discussed in Chapter 1, the atomic masses are given in terms of the nuclear binding energy, $E_B(^{77}\text{Se}^*)$, by:

$$M(^{77}\text{Se}^*) = Zm_p + Nm_n - \frac{1}{c^2}E_B(^{77}\text{Se}^*), \quad (2.3)$$

where m_p and m_n are the masses of the proton and neutron, respectively, Z and N are the numbers of protons and neutrons, respectively, and the star denotes an energetically excited nucleus. A reduction in the nuclear binding energy therefore increases the mass of the target. This increase in nuclear mass is exactly equal to the energy imparted to it scaled by c^2 . As a result, Equation 2.2 for the elastic case can be modified to describe the inelastic case by accounting for the increased mass of the recoil nucleus and the corresponding kinetic energy it takes from the ejectile to do so. Hence, $E_t = E_0 - E - E_N$, where E_N is the nuclear excitation energy, and the mass of the target after the collision becomes $M + E_N/c^2$. The resulting solution for the energy distribution is then

$$E(\theta) = \frac{1}{(M + m)^2} \left[2m^2 E_0 \cos^2(\theta) - E_0(m^2 - M^2) - ME_N(M + m) \pm 2mE_0 \cos(\theta) \sqrt{m^2 \cos^2(\theta) - m^2 + M^2 - M \frac{E_N}{E_0}(M + m)} \right]. \quad (2.4)$$

The resulting curves for nuclear states with energies between 0 and 1 MeV are shown in Figure 2.3.

2.2 Experimental Facility

The $^{77}\text{Se}(d,d')^{77}\text{Se}$ experiment was conducted at the Maier-Leibnitz Laboratory (MLL) on the Ludwig-Maximilians Universität (LMU) and Technische Universität München (TUM) joint campuses in Garching, Germany. This facility was chosen because of its ability to produce deuteron beams of the energy needed for this experiment as well as its high-resolution

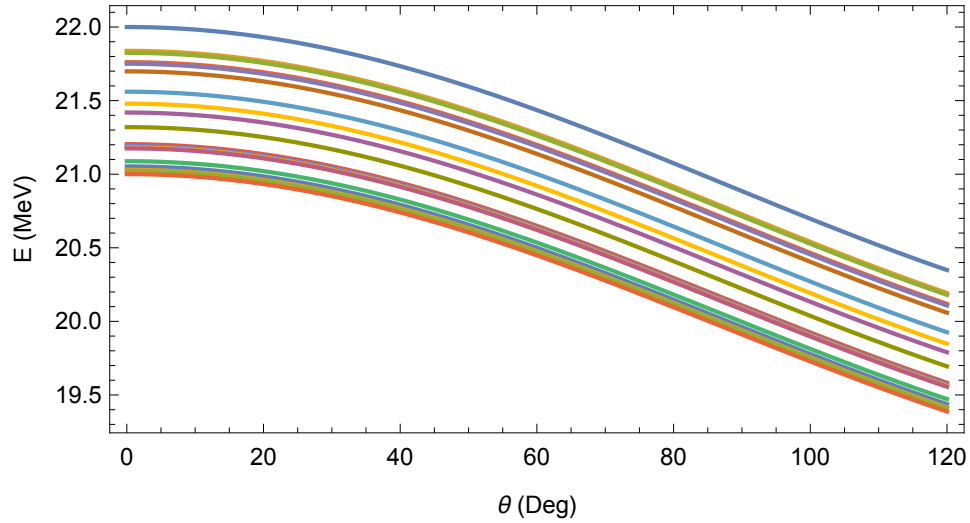


Figure 2.3: Equation 2.4 plotted for deuteron energies following scattering from the excited states of ^{77}Se , $0 < E_N < 1$ MeV. The focal plane receives both these states and the impurity scattering states for low angles (see Figure 2.2).

focal plane detector. The MLL houses a 14 MV Tandem Van de Graaff accelerator which produces various beams of light ions (deuterons, in this experiment). The deuterons are deflected 90° by a large analyzing magnet and sent into the experimental halls. The analyzing magnet also reduces the beam to an energy spread ratio ($\Delta E/E$) of less than 10^{-4} . The tandem accelerator and deflecting magnet used in this experiment are shown in Figure 2.4.



Figure 2.4: Bird's eye view of the tandem accelerator and the analyzing magnet which deflects the beam into the desired experimental hall. The beam is then sent to the target and the magnetic spectrograph. Reproduced from [7].

The tandem accelerator operates like two standard Van de Graaff generators by accelerating negatively-charged ions via a potential difference through a stripper foil which sheds enough electrons to leave the ions singly-positively charged. The same potential that attracted the negative ions sends the resulting positive ions out of the accelerator at high energies (22 MeV for this experiment). A schematic of this style of generator is shown in Figure 2.5.

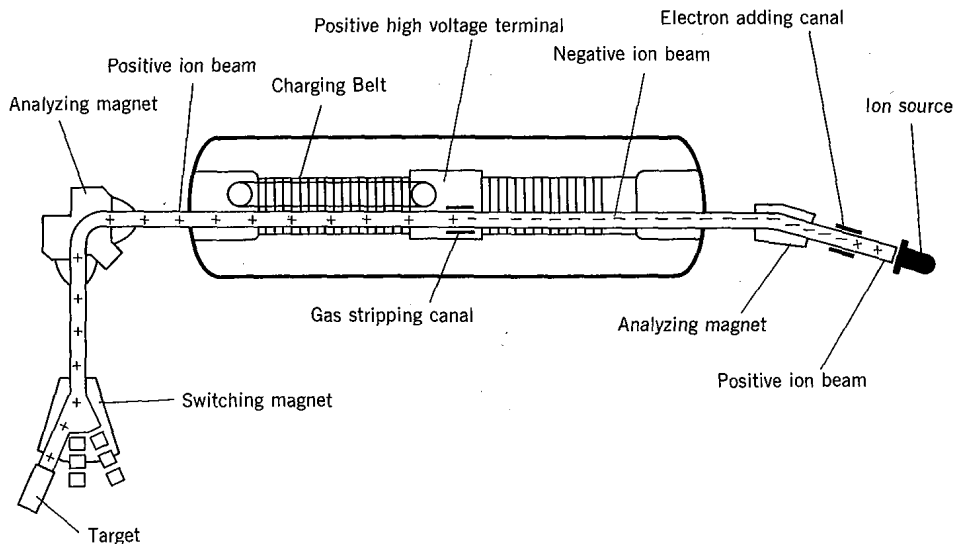


Figure 2.5: Detailed schematic of a standard Van de Graaff generator like the tandem at the MLL. The beam produced here is sent to the analyzing magnet and subsequently into the experimental halls. Adapted from [8].

Once the beam leaves the tandem hall and is deflected into the experimental hall, it reaches the targets. Isotopically enriched targets of $>99\%$ pure ^{77}Se were produced at the MLL for placement on the target ladder, which houses up to five distinct targets and a beam collimator. The target thickness (required for extraction of the cross sections) was determined via deuteron elastic scattering at 15° (see section 4.2). The areal density of the target was taken to be $\sim 100\mu\text{g}/\text{cm}^2$ in all cases. Due to inhomogeneities in the target, a systematic error on the thickness was placed at 5%, which was the leading contribution to the overall uncertainty in most cases. A photograph of the target ladder used in these experiments is shown in Figure 2.6.

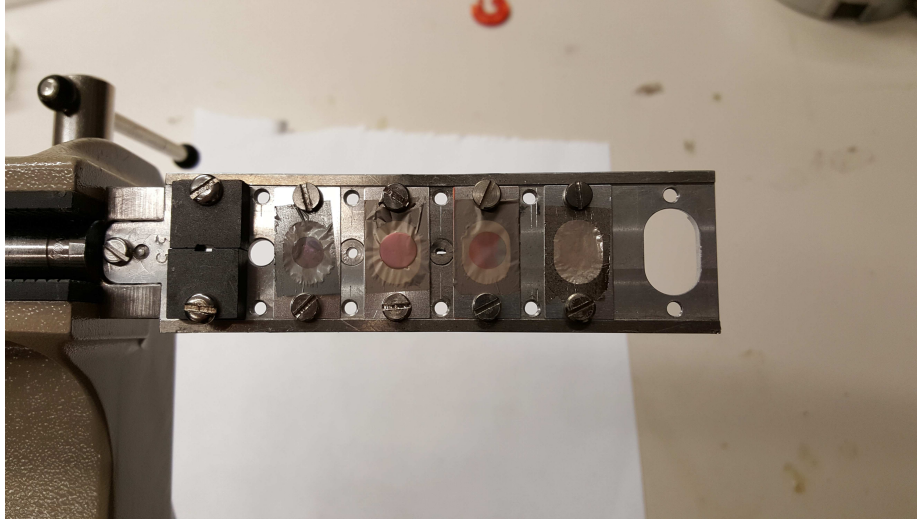


Figure 2.6: Photograph of the ^{77}Se target ladder used in the experiment. The top two slots (right) are not occupied by any targets, the next two slots contain ^{77}Se targets, the next slot contains a target not used in this experiment, and the leftmost portion of the target ladder holds the beam tuning collimator. Picture courtesy of Connor Natzke and Hannah Grover.

After interaction with the target, the reaction products pass through the quadrupole-3-dipole (Q3D) magnetic spectrograph. The Q3D distributes particles across the detector based on their differing radii of curvature from an imposed magnetic field placed normal to their trajectories. The radius of curvature for a given particle depends on its incoming energy and inversely on its charge. A Faraday cup is located behind the target to integrate the non-scattering beam current. Due to the extremely small probability of scattering, this value is effectively the total beam current, and is treated as such. A detailed schematic of the Q3D spectrograph is shown in Figure 2.7.

To detect the reaction products at the Q3D focal plane, a cathode-strip detector determines position and energy loss information and plastic scintillators relay the total energy associated with each event. The former portion of the detector utilizes a gas chamber in which an electron-charge cascade is induced for each event and detected at numerous cathode strips. Signals from these strips are sent to the application-specific integrated circuits (ASICs) for determination of the position at which the event occurred. Finally, the complete deuteron energy is detected by plastic scintillators at the back of the detector. The

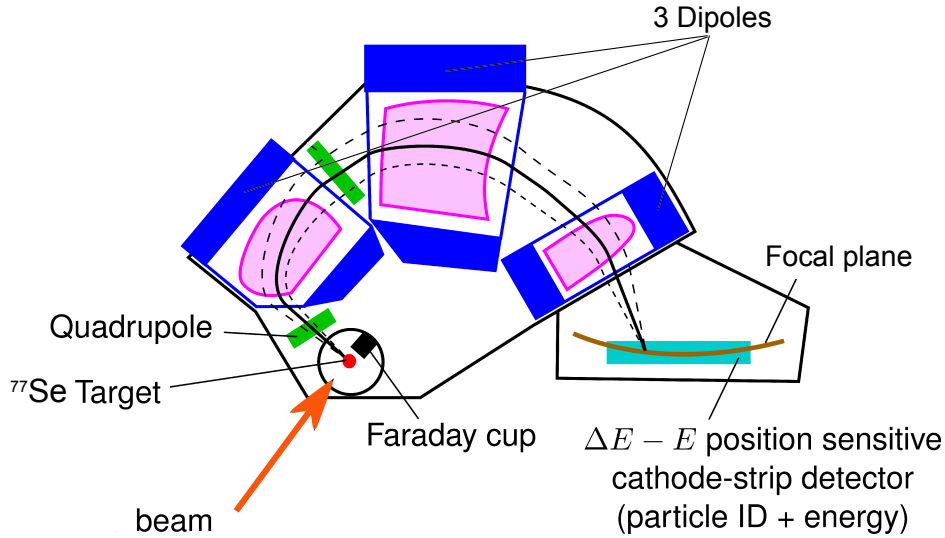


Figure 2.7: A schematic of the Q3D magnetic spectrograph. Beam particles that scatter are sent into the apparatus and curved toward the detector. The Faraday cup reports the beam current for the cross section calculations. The focal plane and Q3D can both be rotated at independent angles. Adapted from [7].

signal from the latter also determines the energy of the particle that caused the event so that plots of total energy versus energy lost can be constructed. This aids in particle identification (discussed in the next section). A schematic of the complete beam path is shown in Figure 2.8.

2.3 Experimental Energy Spectra

The raw data points were first “gated” to extract only deuteron scattering events. This is accomplished by plotting rest energy against energy lost for each particle event at the focal plane. Like particles appear in groups gathered together on this plot and the desired particle species can be isolated by selecting its corresponding group of events on the plot. This procedure was completed at the facility in Germany as the data was gathered. After gating, the raw data files were converted to *.spe* files for further plotting and manipulation.

Once the results were in the *.spe* file type, each run was plotted in *gf3* and each state’s peak was summed and recorded. *gf3* is a spectrum display and fitting program, developed

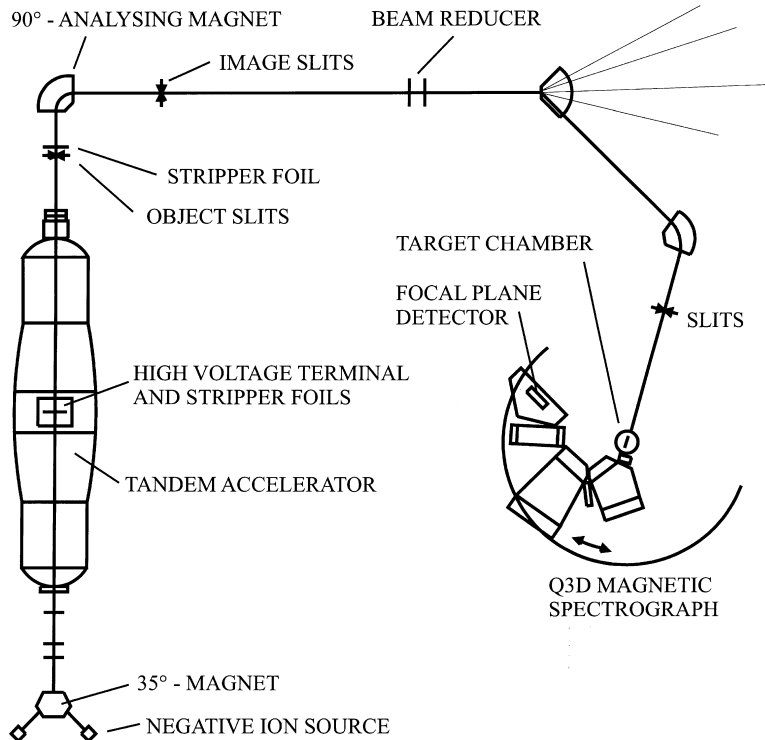


Figure 2.8: A schematic showing the full experimental beam path to the Q3D spectrograph. Adapted from [9].

at Oak Ridge National Laboratory by Dr. David Radford, that allows spectra to be viewed and peaks within them to be integrated [10]. The statistical uncertainties are reported as the square root of the number of counts in the peak. The approximate bin number of each prominent peak centroid was recorded and the counts of each peak were tallied according to this location. Table 2.1 contains the integrated sums of all nine peaks of interest. The experimental energy spectra for all runs performed in this experiment with peaks numbered are shown in the Appendix. Chapter 4 provides a case-by-case discussion of each peak as well as the assignment of state energies to these peaks.

Scattering events on impurities began to enter the focal plane at around 55° . This inhibited summation of the peaks over which it occurred. They continued to move through the focal plane as the angle was decreased until they exited the low-energy side of the focal plane just before the 5° run. Figure 2.9 shows the movement of impurity scattering through the focal plane across various runs.

Table 2.1: Integrated peak counts for nine peaks of interest over all runs. Dashed entries represent peaks that could not be summed because of scattering events on impurities. The corresponding peak numbers are shown on the spectral plots in the Appendix.

Run	$\theta(^{\circ})$	Peak: 1	2	3	4	5	6	7	8	9
92	115	2 834	1 140	1 673	133	171	554	89	166	691
96	110	2 666	1 224	1 749	146	153	598	118	176	580
99	105	4 528	3 935	5717	565	392	1 632	192	432	1 590
100	100	3 078	3 380	4 371	610	245	1 212	169	330	1 110
101	95	8 005	2 756	3 564	578	237	1 007	153	290	1 053
102	90	19 384	3 477	4 725	627	335	1 385	185	332	1 487
103	85	35 889	7 076	10 488	723	600	2 400	355	661	2 666
104	85	10 694	2 143	3 049	199	209	728	72	222	739
115	85	10 450	2 031	3 022	217	182	660	114	184	792
119	85	8 280	1 756	2 702	192	146	612	97	136	648
124	85	7 540	1 446	2 276	148	124	515	68	172	565
136	85	10 745	2 163	3 135	200	184	780	122	188	782
142	85	18 399	3 735	5 312	381	335	1 246	228	286	1 361
143	80	12 601	5 674	8 041	452	350	1 419	210	451	1 501
144	75	10 485	5 351	7 108	620	292	1 210	180	382	1 294
145	70	37 526	4 592	5 717	1 015	347	1 533	235	355	1 342
147	65	70 596	5 659	6 860	1 325	427	1 773	302	455	1 787
148	60	51 235	7 355	10 088	929	367	1 353	284	434	1 323
149	55	96 731	15 668	22 398	1 197	582	2 553	400	784	2 292
150	50	223 394	12 608	17 647	1 369	698	2 676	445	922	2 689
151	45	370 185	12 027	14 260	3 375	921	3 415	569	704	–
152	40	431 103	23 155	29 953	4 369	864	3 570	–	–	–
153	35	1 009 099	27 389	35 609	3 755	923	–	–	–	–
154	30	2 348 392	22 051	27 644	–	–	–	–	–	3 132
155	30	208 547	1 952	2 357	183	114	–	68	124	290
156	25	1 602 201	10 785	–	–	–	1 610	397	611	1 679
157	20	3 262 100	–	–	1 444	424	1 494	391	611	1 447
158	20	123 764	–	1 000	76	–	50	–	–	65
159	15	3 373 370	–	4 002	–	–	355	–	–	285
160	10	–	898	955	–	–	–	–	–	–
161	5	2 750 662	–	–	–	–	–	–	–	–

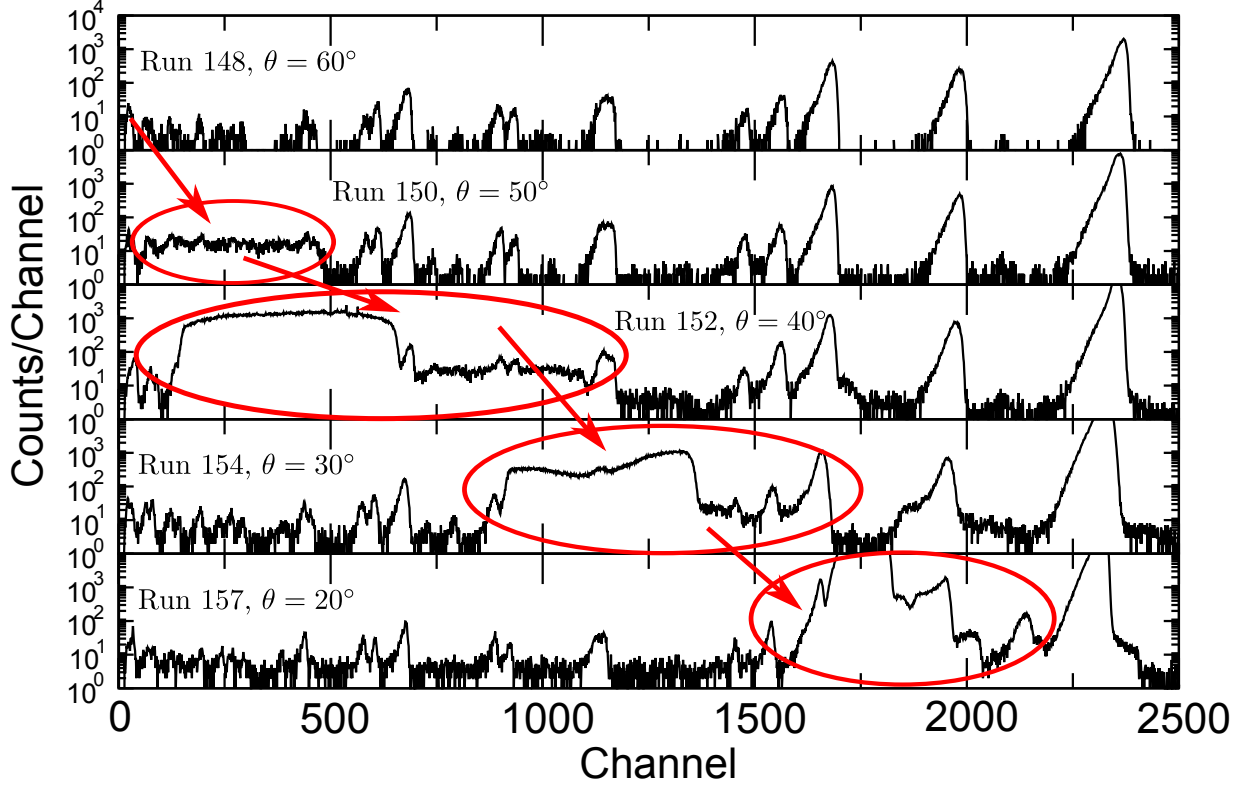


Figure 2.9: Movement of impurity scattering through the focal plane. This scattering eventually left the focal plane again at the 5° run, however, peaks overwhelmed by these events could not be summed.

2.4 Cross Section Extraction

The *cross section* is a reaction-specific quantity that reflects the probability of the reaction occurring. The differential form of the cross section gives this value per unit of solid angle. In this Thesis, an extracted cross section represents the probability of a deuteron scattering on ^{77}Se at its associated angle, energy and populated nuclear state. The experimental determination of the differential scattering cross section for a particular state and scattering angle is [7]:

$$\left(\frac{d\sigma}{d\Omega}\right)_{lab} = \frac{N_c}{N_{t_{eff}} \Delta\Omega N_b L T_1 L T_2} \cdot 10^{34} \text{ (}\mu\text{b/sr)} \quad (2.5)$$

where N_c is the number of counts in the peak, $N_{t_{eff}}$ is the effective number of particles per area in the target, $\Delta\Omega$ is the solid angle coverage of the Q3D spectrograph, N_b is the beam

current, and the LT factors are two live-time ratios. The effective target particle density was estimated from its proposed mass area-density, ρ , with

$$N_{t_{eff}} = \rho(\mu\text{g}/\text{cm}^2) \cdot \frac{10^4 \text{ cm}^2}{\text{m}^2} \cdot \frac{\# \text{ particles}}{g} \cdot \frac{1 \text{ g}}{10^6 \mu\text{g}} = \rho \cdot 10^{-2} \cdot \frac{N_A}{M} \quad (2.6)$$

where ρ was taken to be $100 \mu\text{g}/\text{cm}^2$, N_A is Avogadro's number and M is the molar mass of ^{77}Se . The solid angle acceptance through the slits of the Q3D is set before each run.

The first dead-time contribution is associated with events that occur while the integrated circuits are still processing charge from a previous event in the detector. The counts that occurred during processing were tallied into channel 0 of the gated energy spectrum. The first dead time is the ratio of these uncounted events to the total number and hence LT_1 is given by

$$LT_1 = 1 - \frac{Ch0 \text{ Counts}}{\text{Total Counts}}. \quad (2.7)$$

The second source of dead time addresses the ability of the DAQ to record events. The software records "scalar" (Sc) values which encode missed events during processing. The live-time associated with this process was computed by

$$LT_2 = 1 - \frac{Sc3}{Sc1}, \quad (2.8)$$

where Scalar 3 gives the number of uncounted events by the software and Scalar 1 gives the total number of incident particles based on the beam current, N_b , detected at the Faraday cup. The beam current is determined from the first scalar value according to

$$N_b = \left(\frac{Sc1}{1000} \right) \left(\frac{2 * 10^{-6} \text{ A}}{q} \right), \quad (2.9)$$

where q is the integrated charge and the $2 \mu\text{A}$ value is set experimentally.

The peak areas extracted in the previous section, in addition to the experimental scalars, Q3D angles, target angles, channel 0 values, and total count numbers, were gathered into individual text files for computation of the cross sections. These quantities are displayed in Table 2.2.

Table 2.2: Data and parameters for each run number used in the extraction of the cross sections. Blank cells have the same value as the entry above them.

Run	Target #	$\theta_{Q3D}(\circ)$	Sc1	Sc3	Ch0	Total Counts	$\Delta\Omega$ (msr)
92	T4	115	620 222	943	601	9 617	14.058
96		110	746 844	865	513	9 326	
99		105	1 321 334	2 972	1 625	23 664	
100		100	1 078 909	2 507	1 310	17 968	
101		95	860 695	2 346	1 525	20 927	
102		90	952 887	2 910	2 509	36 450	
103		85	1 061 453	4 133	4 539	68 349	
104	T3	85	135 174	311	457	19 341	
115		85	190 970	382	438	18 896	
119		85	148 303	253	313	15 510	
124		85	135 869	218	249	13 662	
136		85	194 326	409	459	19 570	
142		85	244 830	636	840	33 559	
143		80	254 964	632	932	33 394	
144		75	205 253	545	767	29 610	
145		70	210 336	738	1 377	56 575	
147		65	191 731	994	2 333	94 560	
148		60	120 536	841	1 947	77 516	
149		55	185 338	1 345	4 352	153 056	
150		50	199 280	2 354	7 575	280 460	
151		45	199 788	6 362	54 260	779 190	
152		40	159 330	8 936	38 535	1 160 157	
153		35	134 308	11 388	58 450	1 518 501	
154		30	145 016	26 000	141 811	2 772 324	
155		30	28 371	1 992	9 610	233 765	5.748
156		25	152 766	19 007	124 707	2 609 022	
157		20	168 607	53 850	563 676	7 437 344	
158		20	22 616	2 020	12 313	276 759	1.077
159		15	149 526	42 964	402 151	5 689 378	
160		10	104 728	48 873	1 164 920	9 810 521	
161		5	56 715	19 212	994 535	3 751 862	

According to the prescription of Ref. [7], the center of mass (CM) corrections for the angles and cross sections, respectively, are:

$$\theta_{CM} = \arctan \left(\frac{\sin(\theta_{lab})}{\cos(\theta_{lab}) - \frac{m_p}{m_t}} \right) \quad (2.10)$$

$$\left. \frac{d\sigma}{d\Omega} \right)_{CM} = \left. \frac{d\sigma}{d\Omega} \right)_{lab} \left[1 + \frac{m_p}{m_t} \cos(\theta_{lab}) \right] \left[1 + \left(\frac{m_p}{m_t} \right)^2 + 2 \left(\frac{m_p}{m_t} \right) \cos(\theta_{lab}) \right]^{-3/2}. \quad (2.11)$$

These corrections were employed in reporting the final experimental angular distributions.

2.5 Cross Section Normalization

During the course of the experiment, practical factors, such as a change of target (which introduces a slightly different target thickness) and a detector slit change (which causes a change in the solid angle coverage of the detector), required a normalization procedure. The latter is a physical diminution of the opening size which is performed for smaller angles to ensure that the detector is not overwhelmed with the high particle interaction rate. Although the acceptance size of the detector is known in principle, hysteresis in the apparatus leads to deviations from the experimentally-set value. In this experiment, a target change occurred in one of the 85° runs and slit changes occurred on the second 30° run and the second 20° run. For each of these changes, the subsequent data points were scaled by the ratio of the cross section value after the change to that before the change at the same angle. Figure 2.10 shows the effect of this normalization on the measured angular distribution for elastic scattering. The same normalization factors obtained for the ground state data were applied to the excited states without deducing new ratios, as this method is more reliable than finding new scaling factors for each state.

There were six runs taken at 85° due to ongoing issues with the current integrator as well as a possible suspicion that the target was evaporating selenium. Ultimately the results returned to expected behavior, however there was unexplained variation in the peak count values within these six runs. Namely, the ground state cross section value fell respectably

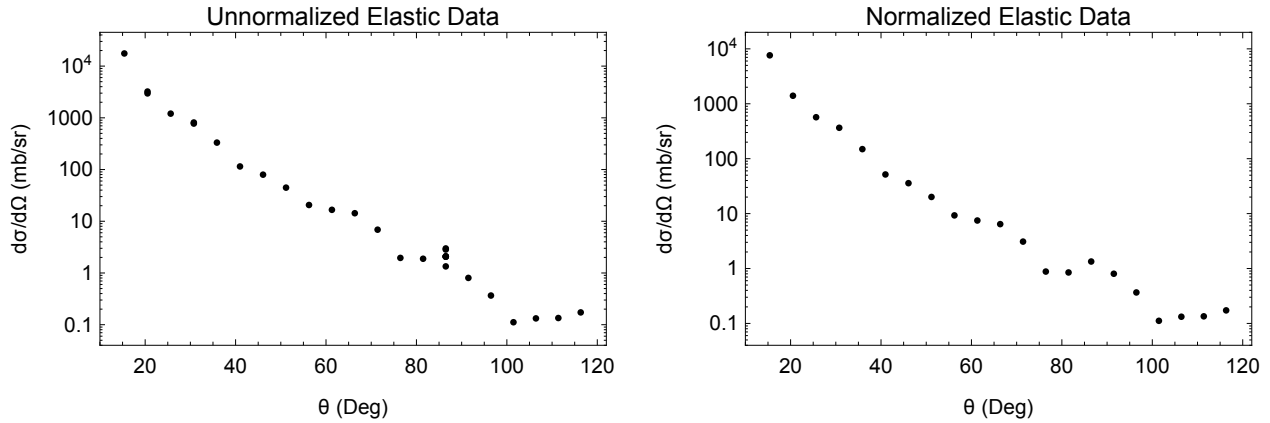


Figure 2.10: Extracted elastic scattering angular distributions a) before and b) after the described normalization procedure. Error bars have been suppressed in this figure to show the detail in the unnormalized plot of repeated-angle data points.

after the first run at 85° , stayed low for the next four runs, and returned on the sixth. Although the reason for this behavior is unknown, it is believed that subsequent data points were not negatively affected by this occurrence and that the surrounding cross section values are trustworthy. A visual depiction of this behavior for the 85° runs is given in Figure 2.11. The normalized angular distributions are shown in Figure 2.12.

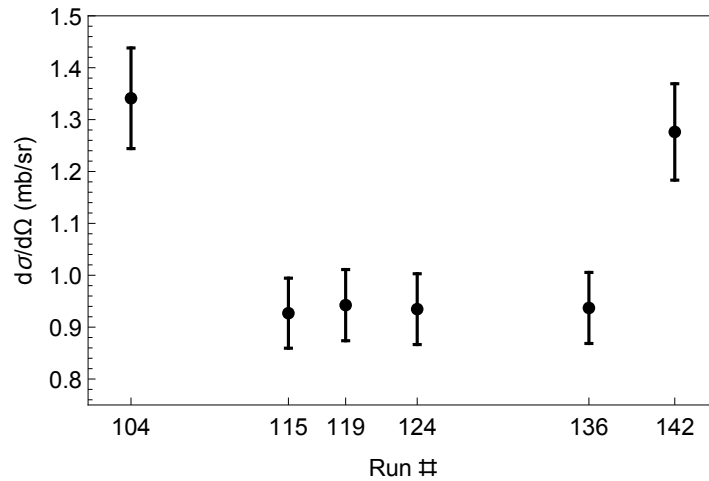


Figure 2.11: Unusual behavior during the 85° runs. The extracted cross section value falls appreciably after the target change at run 104 but returns at run 142. It is not believed that this had an impact on subsequent data, however, because the results appear to have returned to where they were before this occurrence. Runs between those depicted here pertained to another experiment unrelated to the one described in this Thesis.

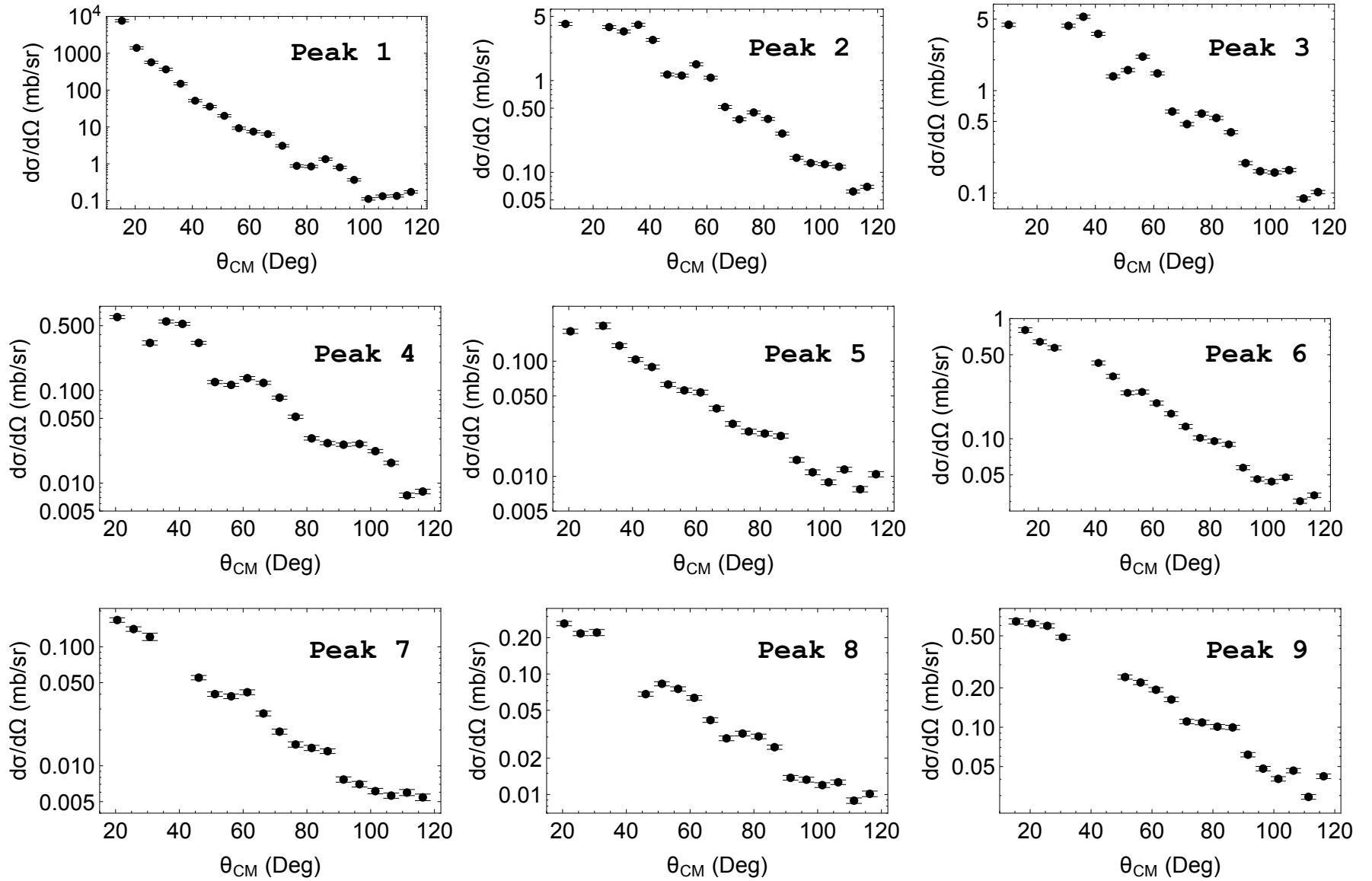


Figure 2.12: Normalized angular distributions for the nine peaks considered in this work. The locations of the peaks in the experimental energy spectra, as numbered in this figure, are shown in the Appendix.

2.6 Energy Calibration

An initial energy assignment to the observed states was attempted by approximating the focal plane energy dependence as linear. After a poor resulting agreement between states and peak locations, it was determined that the first excited state was not the 162 keV state as originally suspected from [11], but rather the 239 and 250 keV doublet (see Chapter 4). The energy difference between this peak and the ground state was divided by the number of bins between them to give the slope of the linear relationship, which was subsequently applied to the remaining peaks by channel number. Using this new linear prescription according to the 239 and 250 keV doublet (see Figure 2.13) produced a much better agreement between the peaks and known states. Confirmation of these assignments was performed via a comparison of the experimental results to both the FRESCO calculations and to previously-measured data listed in the Evaluated Nuclear Structure Data File [12]. The resulting level assignments of the first nine peaks are listed in Table 2.3 and discussed individually in Chapter 4.

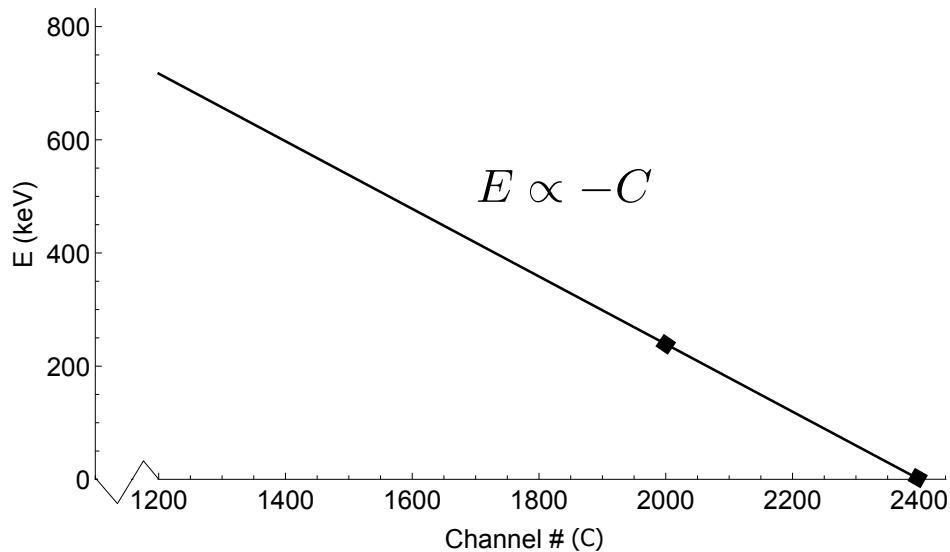


Figure 2.13: Linear calibration scheme used in the preliminary assignment of energy values to focal plane channels. The proportionality constant was determined from the separation between the ground state at bin 2400 and the first excited state (239, 250 keV doublet) at bin 2000. From this ratio, the remaining peaks were assigned energies. Note that lower-numbered bins are assigned events with greater energy and vice versa.

Table 2.3: Assignment of populated states to the peaks in the $^{77}\text{Se}(d,d')^{77}\text{Se}$ experiment. Items in parentheses are presumed by ENSDF [12] according to current data but are not certain. Contributions from states followed by a † were ignored altogether (see Chapter 4).

Peak	E (keV)	J^π
1	0.00	$1/2^-$
2	239.00	$3/2^-$
	249.79	$5/2^{-\dagger}$
3	439.45	$5/2^-$
4	520.64	$3/2^-$
5	581.01	$7/2^-$
6	796.15	$7/2^{(+)\dagger}$
	808.19	$7/2^-$
	817.86	$1/2^{-\dagger}$
	824.43	$(5/2)^{-\dagger}$
7	978.30	$9/2^-$
8	1 005.18	$3/2^-$
9	1 172.49	$9/2^-$

CHAPTER 3

COUPLED-CHANNEL CALCULATIONS WITH FRESCO

Before the β deformation parameters can be extracted from the experimental data, a comparison of the theoretical calculations to the state-by-state angular distributions is required. The underlying framework for calculation in this Thesis is the distorted-wave Born approximation (DWBA) using an optical model potential (discussed next). The program FRESCO was used to calculate predicted cross section values based on the optical model parameters and couplings (section 3.2). SFRESCO was used to perform the global minimization for finding the best coupling strengths (section 3.3).

3.1 Scattering Theory

The Lippmann-Schwinger equation gives the quantum mechanical relationship between the total wave function of scattering, $|\psi_{tot}\rangle$, the incoming projectile wave function, $|\psi_{inc}\rangle$, and the effective scattering potential \hat{V} for an elastic scattering event:

$$|\psi_{tot}\rangle = |\psi_{inc}\rangle + \frac{\hat{V}}{E - \hat{H}_0 + i\epsilon} |\psi_{tot}\rangle, \quad (3.1)$$

where E is the scattered energy, \hat{H}_0 is the free-particle Hamiltonian, and ϵ is a small parameter¹ [13]. Upon inserting a complete set of momentum eigenstates, choosing an appropriate outgoing-wave Green's function, and simplifying, the total wave function is rewritten as

$$\psi_+(\vec{r}) = \psi_{inc}(\vec{r}) - \frac{2m}{\hbar^2} \int \frac{d\vec{r}'}{4\pi|\vec{r} - \vec{r}'|} e^{+ik|\vec{r} - \vec{r}'|} V(\vec{r}') \psi_+(\vec{r}') \quad (3.2)$$

where $\psi_+(\vec{r})$ is the total wave function with the outgoing spherical-wave Green's function such that the exponent is positive.

¹This imaginary portion precludes the fraction from diverging and also gives rise to other interesting phenomena when analyzed with complex number theory.

For a small potential range, r , and large detector and source distances compared to r , the difference $|\vec{r} - \vec{r}'|$ can be simplified:

$$|\vec{r} - \vec{r}'| = \sqrt{r^2 - 2\vec{r} \cdot \vec{r}' + r'^2} \approx r \left[1 - \frac{1}{2} \left(\frac{2\vec{r} \cdot \vec{r}'}{r^2} \right) \right] = r - \hat{r} \cdot \vec{r}' \quad (3.3)$$

because the last term in the radical is of second order in \vec{r}' . Therefore,

$$\frac{e^{ik|\vec{r}-\vec{r}'|}}{e^{|\vec{r}-\vec{r}'|}} \approx \frac{e^{ikr}}{r} e^{-ik\hat{r} \cdot \vec{r}'} \quad (3.4)$$

and Equation 3.2 becomes

$$\psi_+(\vec{k}) = \psi_{inc}(\vec{k}_{inc}) + f(\vec{k}, \vec{k}') \frac{e^{ikr}}{r}, \quad (3.5)$$

where the wavevector \vec{k} is simply the original vector \vec{r} scaled by the wavenumber k . The function $f(\vec{k}, \vec{k}')$ is known as the *scattering amplitude* and immediately gives the differential cross section:

$$\frac{d\sigma}{d\Omega} = |f(\vec{k}, \vec{k}')|^2. \quad (3.6)$$

According to the construction of Equations 3.2 and 3.5, then, the scattering amplitude is related to the scattering potential in the following way:

$$f(\vec{k}, \vec{k}') \propto \langle \vec{k}' | \hat{V} | \psi_+ \rangle. \quad (3.7)$$

Equation 3.2 (and therefore Equations 3.5 and 3.7) is an integral equation for the total wave function, $\psi_+(\vec{r})$, because it appears both inside and outside of the integral. For complicated potentials, this is not easily solved, even with numerical methods. Therefore, the *Born approximation* is made by replacing $\psi_+(\vec{r})$ with $\psi_{inc}(\vec{r})$ inside the integral. This is a first-order approximation for the scattering amplitude and is very suitable for high projectile energies and/or low scattering potentials.

3.1.1 The Distorted-Wave Born Approximation

It is common practice to approximate the incoming and outgoing wave functions as free-particle planewaves, $e^{i\vec{k} \cdot \vec{r}}$. However, a better approximation is a “distorted wave”, which is

treated as a perturbation to the above planewave description. The forms of the distorted waves, $\chi^\pm(\vec{k}, \vec{r})$, used in this Thesis [7] are asymptotically similar to those obtained above for the total wave function:

$$\chi^\pm(\vec{k}, \vec{r}) \rightarrow e^{i\vec{k}\cdot\vec{r}} + f(\theta) \frac{e^{\pm ikr}}{r}, \quad (3.8)$$

where θ is the angle between the incoming trajectory, \vec{k} , and the scattered trajectory, \vec{k}' . These distorted waves (χ^+ for the incoming trajectory and χ^- for the outgoing) account for the specific shape of the nuclear scattering potential (and therefore of the nucleus itself). The resulting transition amplitude, which is directly tied to the β deformation parameters, is [7]:

$$\tau = \int \chi^-(\vec{k}_{scat}, \vec{r}_{scat}) \langle \psi_R \psi_{scat} | \hat{V} | \psi_T \psi_{inc} \rangle \chi^+(\vec{k}_{inc}, \vec{r}_{inc}) dr_{inc} dr_{scat}, \quad (3.9)$$

where the indices *inc* and *scat* are of the incoming and outgoing deuteron, respectively, and *T* and *R* of the target and ejectile. In this case, the potential causing the distortion of the waves in Equations 3.7 and 3.9 is that of the optical model.

3.1.2 The Optical Model

The scattering potential studied exclusively in this Thesis is that of the *Optical Model*, which is a combination of real and imaginary terms:

$$U(r) = V(r) + iW(r). \quad (3.10)$$

This model approximates the nuclear potential with the introduction of both standard and absorptive terms. $V(r)$ models standard elastic scattering and $W(r)$ accounts for absorption of the partial waves by the nucleus.

$V(r)$ is often chosen to match the standard potential of the nucleus: a so-called *Woods-Saxon* potential. It takes the form

$$V_{ws}(r) = \frac{-V_0}{1 + e^{\frac{r-R}{a}}} \quad (3.11)$$

where R gives the mean radius of the potential, a determines the mean “skin thickness”, $4a \cdot \ln(3)$ (the distance over which the potential changes from $0.9V_0$ to $0.1V_0$), and V_0 is the depth of the well [1]. This improvement on the square well treatment of the nucleus gives a more accurate representation of the interior. Such a potential is shown in Figure 3.1 along with its derivative (discussed next).

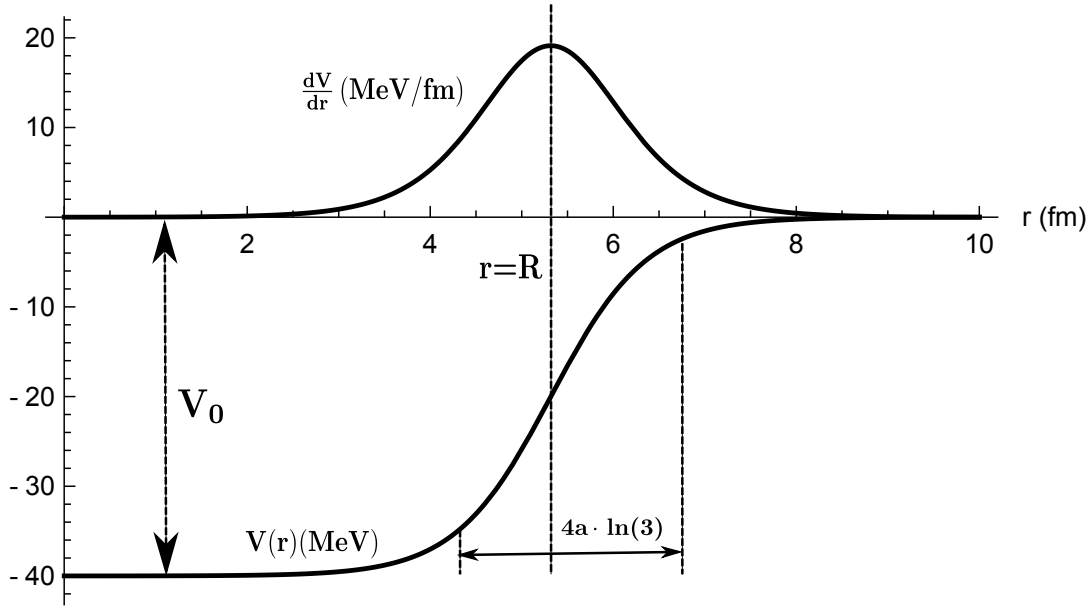


Figure 3.1: The Woods-Saxon potential and its derivative. Note that at the “surface” of the nucleus, when the potential begins to closely approach zero, the derivative is maximal.

The imaginary part of $U(r)$, $W(r)$,¹ must be chosen to account for the absorptive effects of the nucleus, however, these interactions occur primarily on its surface because the Pauli exclusion principle precludes interior non-valence nucleons from absorbing incident nucleons [1]. Because the Woods-Saxon potential has its most abrupt change at the surface and little change in the middle and outside, a derivative of this potential (also shown in Figure 3.1) serves as a great choice for this contribution to $W(r)$. A volume Woods-Saxon term is also added to $W(r)$ to capture any interior effects. Other terms are frequently added to this construction as well including a *spin-orbit* term² which also peaks on the surface (because

¹Note that by definition, then, $W(r)$ itself is real.

²All of the global OMP sets considered in this Thesis use a real spin-orbit term, but one of them also includes a contribution to the imaginary term $W(r)$ (see Table 3.1).

the net spin inside of the nucleus vanishes) and a piecewise *Coulomb* term for reactions with charged projectiles like the deuteron. The latter takes the form

$$V_C(r) = \begin{cases} \left(\frac{ZZ'e^2}{2R_c} \right) \left(3 - \frac{r^2}{R_c^2} \right), & r \leq R_c \\ \frac{ZZ'e^2}{r}, & r > R_c \end{cases} \quad (3.12)$$

where e is the fundamental charge, R_c is the charge radius (chosen to be $1.2A^{1/3}$ fm) and Z and Z' are the target and projectile atomic numbers, respectively. The complete optical model potential is therefore [7]

$$V(r) = -V_v f_r(r) - iW_v f_v(r) + i4W_s a_s \frac{df_s(r)}{dr} + \lambda_\pi^2 \frac{V_{so} + iW_{so}}{r} \frac{df_{so}(r)}{dr} \vec{\sigma} \cdot \vec{\lambda} + V_C(r) \quad (3.13)$$

where $f_x(r)$ is the unscaled Woods-Saxon potential, $(1 + e^{(r-r_x)/a_x})^{-1}$, with specific parameters (r and a) indexed by the subscript on f . The factor of 4 in the symmetry term is conventional. The dot product $\vec{\sigma} \cdot \vec{\lambda}$ is the non-dimensional representation of the spin-orbit coupling $\vec{\ell} \cdot \vec{s}$.

A chosen set of optical model parameters (OMPs) must be compared to the ground state data to assess each set's compatibility with the model. *Global OMPs* are those obtained by fitting these values over large amounts of data in multiple energy and mass ranges. Four global OMP sets were compared for their suitability to this experiment: Perey and Perey (1976) [14], Bojowald *et al.* (1998) [15], An and Cai (2006) [16], and Han, Shi and Shen (2006) [17]. These sets were chosen because they properly model projectile deuterons at the range of energy considered here (22 MeV). The values of the OMPs from these sets are shown in Table 3.1.

The elastic scattering DWBA calculations that result using each of these parameter sets are compared to the data in Figure 3.2. Each curve in this plot represents a separate calculation made with the corresponding OMP set. Based on its superior agreement with the data (especially at higher angles), the set from An and Cai (2006) was chosen for the calculations that follow for the coupled-channel analysis of the experimental data.

Table 3.1: Global OMPs for 22 MeV deuterons on ^{77}Se . These sets are based on the construction of Equation 3.13. Ultimately the set from An and Cai (2006) was chosen based on its closest agreement with the ground state data. Note that table entries with less than three decimal places reflect the levels of precision associated with the entries to which they correspond. The last three parameters are the imaginary spin-orbit terms included in Han *et al.*

Parameter	Perey and Perey	Bojowald <i>et al.</i>	An and Cai	Han <i>et al.</i>
r_c (fm)	1.15	1.3	1.303	1.698
V_v (MeV)	92.144	87.458	91.559	82.882
r_v (fm)	1.15	1.18	1.150	1.174
a_v (fm)	0.810	0.785	0.773	0.809
W_v (MeV)	-	0.0	2.472	0.417
r_w (fm)	-	1.18	1.328	1.563
a_w (fm)	-	0.785	0.430	0.891
W_s (MeV)	19.680	12.224	10.157	14.149
r_s (fm)	1.34	1.27	1.370	1.328
a_s (fm)	0.68	0.857	0.795	0.656
V_{so} (MeV)	7.	6.0	3.557	3.703
r_{so} (fm)	0.75	0.942	0.972	1.234
a_{so} (fm)	0.5	0.942	1.011	0.813
W_{so} (MeV)	-	-	-	-0.206
r_{wso} (fm)	-	-	-	1.230
a_{wso} (fm)	-	-	-	0.813

3.2 FRESCO

FRESCO is a finite-range, coupled-channel DWBA software created by Ian Thompson (University of Surrey and Lawrence Livermore National Lab) [18]. This program is robust enough to handle an unlimited number of nuclear excitations during the calculation. It uses an iterative routine of solving the non-local interactions which permits large calculations effectively. The version of FRESCO employed here includes a NAMELIST input format that is much more intuitive and convenient than the underlying FORTRAN code that it runs.

FRESCO is called via an *input* file. The first partition utilized in this work specifies general calculation parameters, including the range and step size for the angles used in

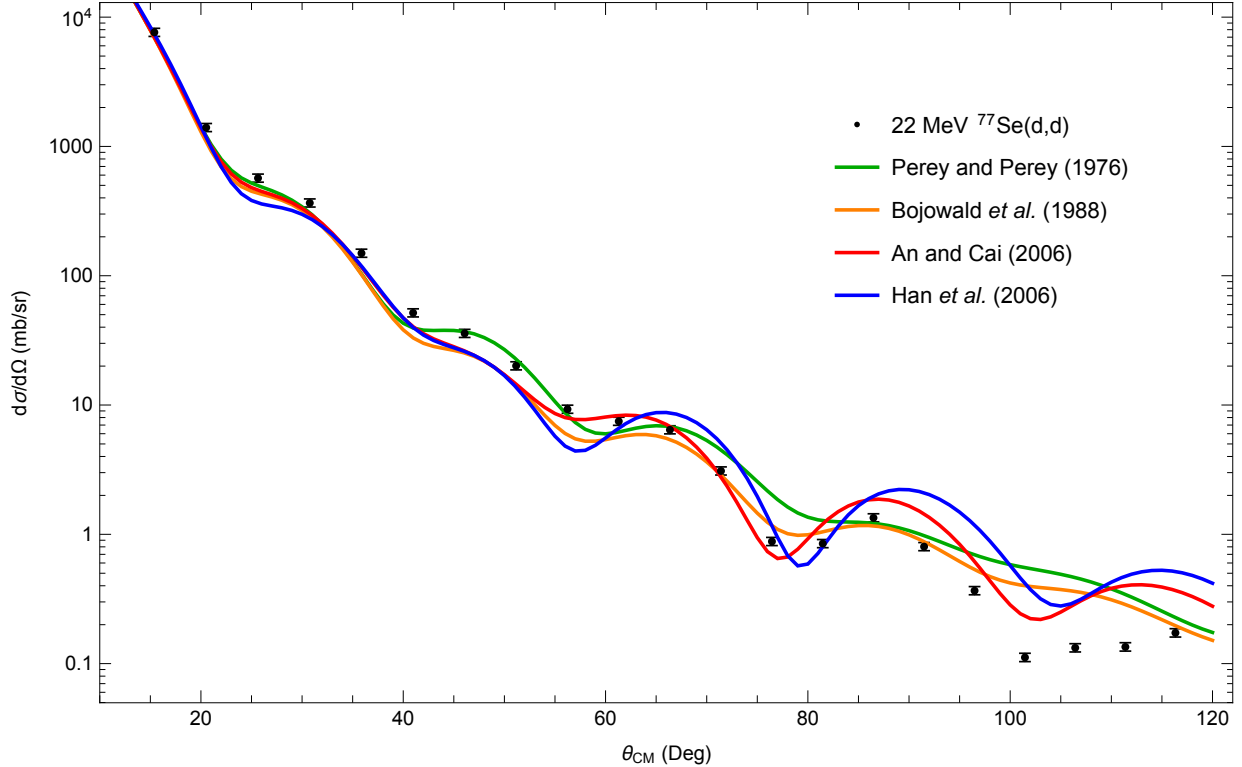


Figure 3.2: A comparison of the DWBA calculations to the elastic scattering data with four different global OMP sets. The set of An and Cai [16] was chosen for subsequent calculations in this Thesis because of its superior agreement with the data; although the set from Perey and Perey does a better job of reproducing the data at lower angles, the set of An and Cai places the extrema much better throughout the entire distribution and therefore is a more appropriate choice overall.

the calculation, the energy of the incoming projectile, and various other coupled-channel settings. The second partition specifies the target and projectile properties including the energies, spins and parities of each target state. Finally, the third partition specifies the optical model parameters and coupling strengths of interest between states. The input file used to find the coupling strengths for the excited states of ^{77}Se is shown in Figure 3.3. Two subsequent partitions also exist for transfer and other more complex reactions and include form factors and sequential transfer information, however, they were not utilized for the work in this Thesis and are not shown in Figure 3.3.

FRESCO produces a large collection of output files after each calculation. The main series of output files are numbered *fort.** and consist of the cross section distributions for

```

77Se(d,d) @ 22 MeV elastic scattering (An06)
NAMELIST
&FRESKO hcm=0.050 rmatch=100.000 jtmin=0.0 jtmax=300.0 thmin=0.00 thmax=-120.00 thinc=1.0
iter=0 iblock=9 chans=1 smats=2 xstabl=2 elab(1)=22.0 /
&PARTITION namep='d' massp=2.0141 zp=1
namet='77Se' masst=76.920 zt=34
qval=0.000 pwf=F nex=9 /
&STATES jt=0.5 bandt=-1 et=0.0000 cpot=1 jp=1.0 bandp=1 ep=0.0000 fexch=F /
&STATES jt=1.5 bandt=-1 et=0.2389988 cpot=1 copyp=1 /
&STATES jt=2.5 bandt=-1 et=0.4394517 cpot=1 copyp=1 /
&STATES jt=1.5 bandt=-1 et=0.5206388 cpot=1 copyp=1 /
&STATES jt=3.5 bandt=-1 et=0.5810106 cpot=1 copyp=1 /
&STATES jt=3.5 bandt=-1 et=0.8081850 cpot=1 copyp=1 /
&STATES jt=4.5 bandt=-1 et=0.9783000 cpot=1 copyp=1 /
&STATES jt=1.5 bandt=-1 et=1.0051838 cpot=1 copyp=1 /
&STATES jt=4.5 bandt=-1 et=1.1724900 cpot=1 copyp=1 /
&partition /
&POT kp=1 type=0 itt=F at=77 rc=1.303 /
&POT kp=1 type=1 itt=F p1=91.5589 p2=1.15 p3=0.773 p4=2.4724 p5=1.328 p6=0.429 /
&POT kp=1 type=-2 itt=F p4=10.1568 p5=1.3697 p6=0.7948 /
&POT kp=1 type=13 itt=F p0=0.01 p2=0.01 p3=0.01 p4=0.01 p7=0.01 /
&STEP ib=2 ia=1 k=2 str=1.0000 /
&STEP ib=3 ia=1 k=2 str=1.2000 /
&STEP ib=3 ia=2 k=2 str=0.4800 /
&STEP ib=4 ia=1 k=2 str=0.3300 /
&STEP ib=4 ia=2 k=2 str=0.2500 /
&STEP ib=5 ia=2 k=2 str=0.5500 /
&STEP ib=6 ia=3 k=2 str=1.5000 /
&STEP ib=6 ia=2 k=2 str=4.2600 /
&STEP ib=7 ia=3 k=2 str=1.3600 /
&STEP ib=8 ia=5 k=2 str=0.6000 /
&STEP ib=8 ia=4 k=2 str=1.1500 /
&STEP ib=9 ia=3 k=2 str=2.3800 /
&STEP ib=8 ia=3 k=2 str=0.6000 /
&STEP ib=8 ia=1 k=2 str=0.6000 /
&step /
&POT kp=1 type=3 itt=F p1=3.557 p2=0.972 p3=1.011 /
&pot /

```

FRESKO Parameters

Nuclear States
Information

Optical Model
Parameters

Distorted-Potential
Couplings

Figure 3.3: FRESKO input file used to produce calculated distributions as well as in the determination of the optimized coupling strengths.

each state, starting with the ground state on *fort.201*. There is also a *.out* file generated which displays the DWBA calculation process and conveys other information pertinent to the calculation. The various *fort.** files were used for plotting the cross section distributions as in Figure 3.2 and for aiding in creating the appropriate SFRESKO input files. An example of the ground state *fort.201* file is shown in Figure 3.4. It consists of plotting information for display in the program GRACE as well as the calculated distributions.

```

# 143 angles, 1 tensor ranks for 0=projectile
@subtitle "77Se(d,d) @ 22 MeV elastic scattering (An06)"
@legend ON
@legend x1 0.2
@legend y1 0.8
@g0 type LOGY
@yaxis ticklabel format power
@legend string 0 "Lab energy = 22.0000"
#legend string 0 "Partition= 1 Excit= 1 near/far= 1"
# Theta      sigma      iT11      T20      T21      T22      Kyy for projectile
0.1000E-01  0.5620E+17
1.000      0.5600E+09
2.000      0.3515E+08
3.000      0.7211E+07
4.000      0.2317E+07

```

} GRACE Plotting Information

} Beginning of Plot Data

Figure 3.4: Sample ground state *fort.201* file using the An and Cai OMP set.

3.3 SFRESCO

SFRESCO runs FRESCO iteratively to find the best chi-square fit of a function and variable(s) to the supplied data. It uses the MINUIT [19] libraries by F. James (Computing and Networks Division, CERN) to process a simultaneous minimization of the relative coupling strengths for each state with respect to the observed data. The coupling strengths between states are labeled *str* in the input file. SFRESCO is called via a *.search* file which identifies the input file to be modified in the minimization, the desired output filename, the variable(s) being optimized (and their corresponding location(s) in the input file), and the data to which the calculations are minimized for each state. A breakdown of this file (as constructed for the final minimization) is given in Figure 3.5.

In addition to the FRESCO output files discussed in the previous section, SFRESCO produces its own output files, the most important of which is the *search.plot* file. This file, also formatted for plotting with GRACE, displays the cross section distributions for each state after the minimization has been achieved as well as the optimized variable values. This file was used to compare the resulting angular distributions to the data (which aids in choosing the appropriate coupling channels) as well as for obtaining the β deformation parameters. A example *search.plot* file is displayed in Figure 3.6.

```

'77Se_An06.in' '77Se_An06.out' 14 9 ——— Number of States/Data Sets
                                     Number of Fitting Variables
&variable kind=1 name='1->2 k=2' kp=1 pline=5 /
&variable kind=1 name='1->3 k=2' kp=1 pline=6 /
&variable kind=1 name='2->3 k=2' kp=1 pline=7 /
&variable kind=1 name='1->4 k=2' kp=1 pline=8 /
&variable kind=1 name='2->4 k=2' kp=1 pline=9 /
&variable kind=1 name='2->5 k=2' kp=1 pline=10 /
&variable kind=1 name='3->6 k=2' kp=1 pline=11 /
&variable kind=1 name='2->6 k=2' kp=1 pline=12 /
&variable kind=1 name='3->7 k=2' kp=1 pline=13 /
&variable kind=1 name='5->8 k=2' kp=1 pline=14 /
&variable kind=1 name='4->8 k=2' kp=1 pline=15 /
&variable kind=1 name='3->9 k=2' kp=1 pline=16 /
&variable kind=1 name='3->8 k=2' kp=1 pline=17 /
&variable kind=1 name='1->8 k=2' kp=1 pline=18 /

&data type=0 data_file='Data/final1data' iscale=2 idir=0 lab=F abserr=T ic=1 ia=1/
&data type=0 data_file='Data/final2data' iscale=2 idir=0 lab=F abserr=T ic=1 ia=2/
&data type=0 data_file='Data/final3data' iscale=2 idir=0 lab=F abserr=T ic=1 ia=3/
&data type=0 data_file='Data/final4data' iscale=2 idir=0 lab=F abserr=T ic=1 ia=4/
&data type=0 data_file='Data/final5data' iscale=2 idir=0 lab=F abserr=T ic=1 ia=5/
&data type=0 data_file='Data/final6data' iscale=2 idir=0 lab=F abserr=T ic=1 ia=6/
&data type=0 data_file='Data/final7data' iscale=2 idir=0 lab=F abserr=T ic=1 ia=7/
&data type=0 data_file='Data/final8data' iscale=2 idir=0 lab=F abserr=T ic=1 ia=8/
&data type=0 data_file='Data/final9data' iscale=2 idir=0 lab=F abserr=T ic=1 ia=9/
&

```

Variable List and Input
File Line Reference

Data Set Paths

Figure 3.5: The `.search` file used to call SFRESKO and specify the fitting variables and excited-state data sets.

3.4 Extraction of β Deformation Parameters

Once the coupling strengths have been obtained from the SFRESKO optimization, they can be used to extract the β deformation parameters. The `str` value in SFRESKO corresponds to the reduced nuclear deformation length of the nuclear state, RDEF, and is directly related to the corresponding β deformation parameter:

$$str = \beta_\lambda * R_0, \quad (3.14)$$

where $R_0 = 1.2 A^{1/3}$ (fm).

```

# Var 1=1->2 k=2 value 0.905294, step 0.0100, error 0.0076
# Var 2=1->3 k=2 value 1.051888, step 0.0100, error 0.0101
# Var 3=2->3 k=2 value 0.096404, step 0.0100, error 0.2498
# Var 4=1->4 k=2 value 0.295900, step 0.0100, error 0.0106
# Var 5=2->4 k=2 value 0.732646, step 0.0100, error 0.0692
# Var 6=2->5 k=2 value 1.071193, step 0.0100, error 0.0142
# Var 7=3->6 k=2 value 0.674132, step 0.0100, error 0.3052
# Var 8=2->6 k=2 value 1.961820, step 0.0100, error 0.0988
# Var 9=3->7 k=2 value 0.855559, step 0.0100, error 0.0128
# Var 10=5->8 k=2 value -0.187738, step 0.0100, error 0.4458
# Var 11=4->8 k=2 value -0.735658, step 0.0100, error 0.3442
# Var 12=3->9 k=2 value 2.176240, step 0.0100, error 0.0279
# Var 13=3->8 k=2 value -1.394802, step 0.0100, error 0.1093
# Var 14=1->8 k=2 value -0.271749, step 0.0100, error 0.0147

```

} Fitted Variable Values

```

# ChiSq/N = 1096.450 from 8571.344 29.044 28.096 16.517 10.131 9.441
# 10.359 3.215 6.209
@subtitle "Search file: 77Se_An06.search; Fresco input: 77Se_An06.in"
@subtitle size 0.7
@legend ON
@TYPE xydy
@legend string 0 "CM set 1:Data/final1data"
@s0 linestyle 0
@s0 errorbar length 0.28
@s0 symbol 2
@s0 color 1
@s0 symbol fill 1
@s0 symbol size 0.5
116.334 0.17289 0.12885E-01
111.386 0.13466 0.10056E-01
106.428 0.13245 0.97525E-02

```

} GRACE Plotting Information For All States

Figure 3.6: The beginning of the *search.plot* file obtained from the SFRESCO calculation. The optimized *str* values and associated errors are given in the first section of the file, followed by GRACE plotting information for both the data and calculations for all of the states specified in the input file.

CHAPTER 4
DISCUSSION AND CONCLUSIONS

4.1 Extracted β Deformation Parameters

The extracted β deformation parameters (according to the scheme shown in Figure 4.1) for the nine states are shown in Table 4.1 and are compared to the values obtained from the electromagnetic transition probabilities on ENSDF. The relationship between the transition probabilities, notated $B(E\lambda)$, and the β deformation parameters, is¹.

$$B(E\lambda) = \left(\frac{3}{4\pi} R_0^\lambda Z \beta_\lambda \right)^2 (e^2 b^\lambda), \quad (4.1)$$

where $R_0 = 0.12A^{1/3} (b^{1/2})$ and λ is the multipolarity of the electric transition, E . Comments on the β values obtained for each state are given in the next section on an individual basis.

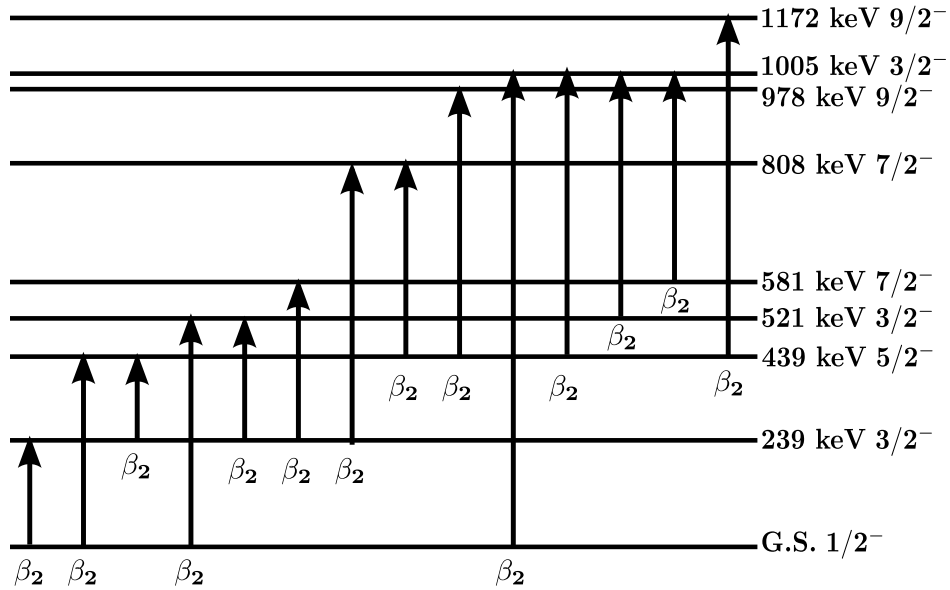


Figure 4.1: Coupling scheme used in the extraction of the β deformation parameters.

¹As adopted from Bohr and Mottelson [20] by Capote [21].

Table 4.1: Extracted β deformation parameters from this Thesis compared to the electromagnetic values on ENSDF [12] (from which the energy values are also taken). All entries are reported as absolute values. The listed uncertainties on the β values obtained in this Thesis are only statistical and contain no systematic contributions.

E_f (keV)	J_f^π	E_i (keV)	J_i^π	λ	$\beta_\lambda^{dd'}$ (This Thesis)	β_λ^{EM} (ENSDF)
238.9988	12	0.0	$1/2^-$	2	0.177(2)	0.200(7)
439.4517	14	238.9988	12	$3/2^-$	$0.019^{+0.049}_{-0.019}$	$0.096^{+0.030}_{-0.028}$
		0.0	$1/2^-$	2	0.206(2)	0.235(7)
520.6388	15	238.9988	12	$3/2^-$	0.144(14)	$0.048^{+0.024}_{-0.020}$
		0.0	$1/2^-$	2	0.058(2)	$0.065^{+0.034}_{-0.040}$
581.0106	17	238.9988	12	$3/2^-$	0.210(3)	$0.107^{+0.011}_{-0.008}$
808.185	3	439.4517	14	$5/2^-$	0.132(60)	$0.292^{+0.116}_{-0.145}$
		238.9988	12	$3/2^-$	0.384(19)	$0.834^{+0.098}_{-0.175}$
978.30	10	439.4517	14	$5/2^-$	0.168(3)	$0.255^{+0.063}_{-0.085}$
1005.1838	20	581.0106	17	$7/2^-$	$0.037^{+0.087}_{-0.037}$	$0.123^{+0.045}_{-0.048}$
		520.6388	15	$3/2^-$	0.144(67)	$0.225^{+0.096}_{-0.114}$
		439.4517	14	$5/2^-$	0.273(21)	–
		0.0	$1/2^-$	2	0.053(3)	–
1172.49	16	439.4517	14	$5/2^-$	0.426(6)	$0.466^{+0.079}_{-0.095}$

4.2 State-by-State Discussion

This section contains a case-by-case discussion of each state including the agreement of the experimental angular distributions with the calculations, the agreement of the extracted β values with their electromagnetic counterparts on ENSDF, and a breakdown of peaks containing several populated states.

- **Ground State $1/2^-$**

As discussed in section 2.5, multiple runs were taken at 85° due to problems with the current integrator and target thickness. Within this series of runs, the target was changed and the subsequent cross section values were normalized to this point.

Normalizations also occurred, for this state and all others, after slit changes at runs 155 and 158. It was also decided that the data point at 5° for the ground state (the only state for which this run could be summed) would be discarded on account of its heavy disagreement with calculation and large dead-time correction at this angle (see Figure 4.2). Overall, the agreement between the ground state data and the calculated elastic distribution is excellent.

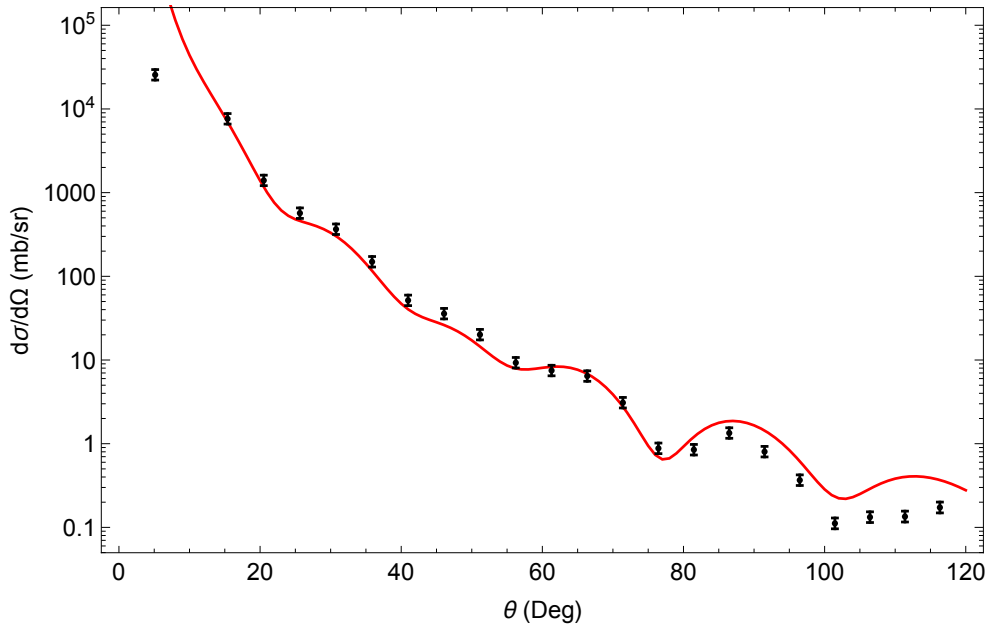


Figure 4.2: Ground state data compared to calculation. In general there is excellent agreement. However, the data point at 5° does not properly fall in line with calculation and was consequently discarded.

- **Unobserved 162 keV State**

Previous work for the $^{77}\text{Se}(d,d')^{77}\text{Se}$ experiment (Ref. [11]) listed a state near 160 keV. A state in near proximity to this is known to exist [12] at 162 keV, however any population of this state in this experiment was below a discernible level. It is therefore concluded that the presence of this peak in the previous experiment was due to impurity scattering or poor detector resolution, as the resolution of the Q3D spectrograph used in this facility is much higher than in previous measurements. Furthermore, this state is a

$7/2^+$ state and no positive parity states were appreciably populated in this experiment (due to the negative parity of the ground state). It is therefore not expected that this state would produce a prominent peak in this experiment.

- **Unresolved 239, 250 keV Doublet**

The first prominent excited-state peak has a width that is too large to separate contributions from the 239 and 250 keV states. However, it appears as though the peak consists mostly (by an order of magnitude) of the lower-energy state because at certain angles, the higher-energy portion begins to be visible on the left with a much smaller peak height (see Figure 4.3), although it is possible that this was instead due to more prominent multiple scattering from this state. Furthermore, due to the lower nuclear spin of the the 239 keV state, population of this state is more probable. It is for these reasons that this peak was treated as only the 239 keV state, an approximation that is likely good to first order. Any contributions from the 250 keV state were neglected during the FRESCO analysis. This state was then coupled to the ground state with an L=2 transfer. The agreement with the calculations is good for lower angles of scattering, however the maxima and minima are missed for higher angles.¹ Subsequent couplings to the ground state of other multiplicities were attempted to improve the agreement, however, they were forbidden by FRESCO's selection rules as expected. The extracted β value to the ground state agreed fairly well with the literature.

- **439 keV $5/2^-$ State**

The 439 keV state was observed as expected and coupled to the ground state and to the 239 keV state with L=2 transitions, also as expected from the evaluated data file [12]. Like the previous state, the agreement with the calculations was strong except at

¹Agreement between the calculations and the extracted angular distributions was assessed primarily qualitatively (location of extrema, overall magnitude, and closeness of data points to the curves), as well as by comparing the extracted β values to the literature. Quantitative comparison with χ^2 values proved to not be useful due to their large magnitudes.

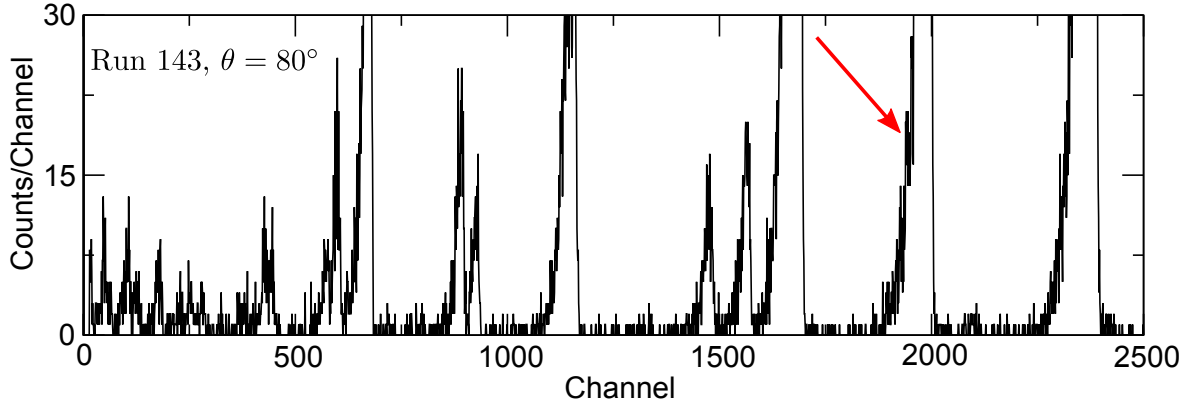


Figure 4.3: Supposed presence of the 250 keV state. It appears that the second, smaller, peak lies to the left of the overall centroid, suggesting that the entire peak mostly consists of contributions from the lower-energy, 239 keV state. Therefore, this peak was summed as though it was only from the 239 keV state.

higher angles and subsequent couplings to the ground state of different multiplicities were attempted without success. Other multiplicities were also attempted for the coupling to the 239 keV state with no success, leaving no remaining couplings to lower states. The β value for the coupling to the ground state agreed well with the literature, however the coupling to the 239 keV state was substantially lower (up to a factor of two). This is in part because the doublet at 239 keV couldn't be resolved, and also because higher-state couplings to the 239 keV state affect this value; upon adding subsequent states to the calculation routine, this value decreased with each additional coupling that included the 239 keV state.

- **521 keV $3/2^-$ State**

The 521 keV state was observed as expected. It was also coupled to the ground state and 239 keV state with $L=2$ transfers. The agreement with the calculations was excellent. The β value to the ground state agreed well with the literature, however the coupling to the 239 keV state was higher by up to a factor of two, likely for similar reasons described earlier in coupling to the 239 keV state.

- **581 keV $7/2^-$ State**

The 581 keV state was observed as expected and coupled to the 239 keV state. It was also confirmed that this state does not have a prominent coupling to the ground state. The agreement with the calculations was very good concerning the location of the maxima and minima, however, the cross section values extracted in the experiment at lower angles were notably less than those obtained in the calculations. This is likely due to the fact that this state has a very prominent coupling to the neglected 250 keV state ($B(E2)(W.u.)=74 \text{ } 2\beta$ according to [12]) and such behavior could not be accounted for in this experiment because the doublet around 250 keV could not be resolved. The β value for the 239 keV coupling was approximately twice that of the literature similarly to the previous state.

- **Unresolved 808 ($7/2^-$), 818 ($1/2^-$), and 824 ($5/2^-$) keV Triplet**

There are actually four states with energies that fall within this peak width, however, contributions from the first of these states (796 keV $7/2^+$) was presumably negligible due to the positive parity. The best agreement with the calculations was obtained when this peak was assumed to be only from the 808 keV state and not from the 818 keV state as initially expected (because the 818 keV state has a lower spin value). Due to the very small separation (<10 keV) between each of these states, they could not be separated and assignment of this peak to only the 808 keV state is not certain. Future couplings down to this state were therefore avoided and the couplings from this state (to the 439 and 239 keV states) produced large uncertainties in the calculation process. There was overlap with the literature in the value obtained for β to the 439 keV state, in part due to the large uncertainties. The value for the 239 keV coupling was as much as half as the literature, however. Furthermore, ENSDF lists a coupling (with no strength specified) between this state and the 250 keV state. This likely contributes to the poorer agreement in this β value.

- **978 keV $9/2^-$ State**

The 978 keV state was observed and coupled to the 439 keV state alone. The agreement with the calculations was good, however, like with the 581 keV state, the cross section values obtained from the calculations at low angles were greater than those actually observed. This state also has a prominent coupling to the neglected 250 keV state ($B(E2)(W.u.)=130\ 70$ in [12]) which accounts for some of the discrepancy. Further couplings to the 581 keV state were attempted without improvement in the distributions or in the β values. The β value for this state agreed with the literature, however, as it contained a large uncertainty.

- **1005 keV $3/2^-$ State**

The 1005 keV state was observed and initially coupled to the 521 and 581 keV states as listed on ENSDF. However, the resulting agreement with the calculations was very poor, and so additional couplings were explored. Subsequently, it was concluded that there is likely an L=2 coupling to the ground state as well as to the 439 keV state. The latter was proposed on ENSDF without a multipolarity, however, the choice of an L=2 transfer, in addition to including coupling to the ground state, produced excellent agreement with the calculations. It was also concluded that there is likely not a prominent coupling to the 808 keV state (due to unreasonable resulting *str* values), in agreement with ENSDF. The two couplings from this state listed on ENSDF agreed with the values obtained in this experiment due to the large uncertainties involved. The other two β values obtained in this experiment were not present on ENSDF.

- **1172 keV $9/2^-$ State**

The final peak was assigned to the 1172 keV state, although placement of these energies began to diverge from the purely linear relationship between channel number and energy as previously employed. However, this assignment ultimately proved to agree

well with the calculations and this state was subsequently coupled to the 439 keV state. The distribution for this state (in both the calculations and the data) was remarkably similar to that of the triplet peak. The β value for the coupling to the 439 keV state agreed well with the literature.

The experimental angular distributions are shown with the calculations for each of the states discussed above in Figure 4.4.

4.3 Conclusions

In conclusion, a 22 MeV inelastic deuteron experiment was performed on targets of ^{77}Se and the ejectiles were momentum-sorted using a Q3D spectrograph at angles ranging from 5° to 115° in increments of 5° . Angular distributions were obtained for the first nine prominent peaks corresponding to excited nuclear states of up to 1173 keV in ^{77}Se . After comparison to the elastic data, the OMP set from An and Cai was chosen to complete a coupled-channel calculation with respect to the data and find the minimum- χ^2 β_2 deformation parameters. The coupling scheme of Figure 4.1 was used to extract 14 of these β values and the results were compared to the electromagnetic values listed on ENSDF (Table 4.1).

The overall agreement between the calculated and extracted angular distributions is good, with no substantial deviations. The 239, 439, 581 and 978 keV states express a systematic rise above the calculated cross section values at low angles, however the extrema are well-located. Furthermore, there appears to be a deviation in the location of the extrema for the 239 and 439 keV states. There appear to be no substantial complications from peaks that could not be resolved and the approximation of the second peak as solely the 239 keV state and the sixth peak as solely the 808 keV state appears to be valid; however, the inability to resolve the 250 keV state appears to affect some of the couplings involving this state. The agreement between the extracted β deformation parameters and those obtained from ENSDF varies. There is good agreement for the more well-known values including the 239 keV to ground, 439 keV to ground, and 1172 to 439 keV couplings. Some of the large uncertainties

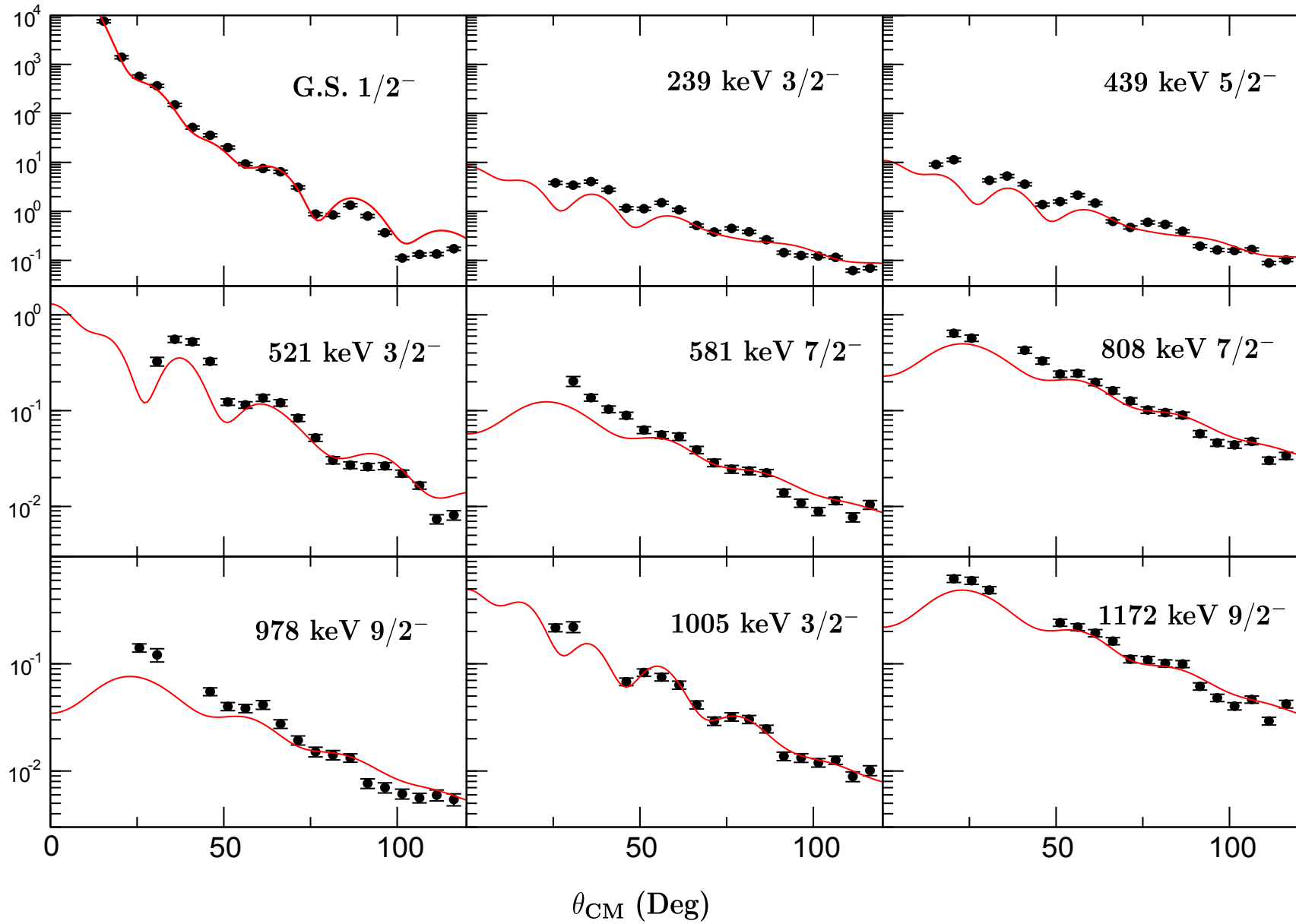


Figure 4.4: Experimental angular distributions with the corresponding calculations (according to the scheme in Figure 4.1 and β values in Table 4.1) overlaid. In general, the agreement obtained is very good, with slight deviations at low angles and a few extrema locations of poor agreement in the 239 and 439 keV states.

in both this work and in the literature provide overlap in the β values (such as for the 808 to 439 keV and the 1005 to 521 keV transitions). Other values deviate by factors of two or more, including the 439 to 239 keV and 521 to 239 keV transitions. It is likely that some of the deviations are because the 581 and 978 keV states (and possibly the 439 keV state) have prominent couplings to the 250 keV state, which could not be resolved and accounted for in this experiment. One particular discrepancy of interest is that of the 439 to 239 keV transition, which deviated from the literature by as much as a factor of two (due to the large uncertainty for this value in this work).

Implementation of these β values to refine the theoretical structure calculations for closely-related nuclei (such as ^{76}Se , the daughter nucleus in the ^{76}Ge $\beta\beta$ decay modes) will provide more accurate guidance for the Nuclear Matrix Elements of this region. In-depth study of the various modes of $\beta\beta$ decay with these refined NMEs can shed light on the mass characteristics of the neutrino, as well as possible necessary extensions to the Standard Model.

REFERENCES CITED

- [1] Kenneth Krane. *Introductory Nuclear Physics*. Wiley, 1987.
- [2] C. Patrignani *et al.* (Particle Data Group). *Chin. Phys. C*, 2016, **40**(10): 100001, 768 (2016).
- [3] Y. Fukuda *et al.* Evidence for oscillation of atmospheric neutrinos. *Phys. Rev. Lett.*, **81**:1562–1567, Aug 1998. doi: 10.1103/PhysRevLett.81.1562.
- [4] Q. Ahmad *et al.* *Phys. Rev. Lett.*, 89:011301, 2002.
- [5] J. Menéndez. What do we Know About Neutrinoless Double-Beta Decay Nuclear Matrix Elements? arXiv:1605.05059v1 [hep-ph], 2015.
- [6] M. Agostini *et al.* *Phys. Rev. Lett.*, 111:122503, 2013.
- [7] Leach, Kyle G. (2012). *Neutron Transfer Reactions on ^{64}Zn as a Probe for Testing Shell-Model Isospin-Symmetry-Breaking Theory* (Doctoral dissertation). Retrieved from https://www.physics.uoguelph.ca/Nucweb/theses/KGL_PhD_Thesis.pdf.
- [8] R.J. Van de Graaff. *Nucl. Instrum. and Meth.* **8**, 195 (1960).
- [9] O. Schmelmer *et al.* *Nucl. Instrum. and Meth. in Phys. Res. B* **142**, 210-213 (1998).
- [10] D. C. Radford. Gf3 Peak-Fitting and Plotting Program, Unpublished (2000).
- [11] B. Singh and N. Nica. *Nuclear Data Sheets*, 113(5): 1115-1314 (2012).
- [12] Evaluated Nuclear Structure Data. <http://www.nndc.bnl.gov/ensdf>.
- [13] J. J. Sakurai and Jim Napolitano. *Modern Quantum Mechanics*. Pearson, 1994.
- [14] C.M. Perey and F.G. Perey. *Atom. Data and Nucl. Data Tables* **17**, 1-101 (1976).
- [15] J. Bojowald *et al.* *Phys. Rev. C* **38**, 1153 (1988).
- [16] Haixia An and Chonghai Cai. *Phys. Rev. C* **73**, 054605 (2006).
- [17] Yinlu Han, Yuyang Shi, and Qingbiao Shen. *Phys. Rev. C* **74**, 044615 (2006).

- [18] Ian J. Thompson. FRESCO Coupled-Channel DWBA Program, Version 2.9, Unpublished (2011).
- [19] F. James. MINUIT - Function Minimization and Error Analysis, Unpublished (1998).
- [20] Aage Bohr and Ben Mottelson, *Nuclear Structure*, World Scientific Publishing (1969).
- [21] R. Capote *et al.*, Nuclear Data Sheets **110**, 3107 (2009).

APPENDIX
EXPERIMENTAL ENERGY SPECTRA

